MULTISCALE MODEL. SIMUL.
Vol. 23, No. 4, pp. 1551–1580

AN ITERATIVE METHOD BASED ON GENERALIZED MULTISCALE FINITE ELEMENT METHODS FOR PARAMETER-DEPENDENT DUAL CONTINUUM MODEL*

QIUQI LI†, LINGLING MA‡, AND PINGWEN ZHANG§

Abstract. In this paper, we consider an iterative method based on the generalized multiscale finite element method (GMsFEM) to solve the dual continuum model with random inputs. The main idea of iterative methods is to reformulate the original model into another model with parameter-independent diffusion coefficients and parameter-dependent right-hand sides. Subsequently, a fixed-point iteration is used to compute the solution of the reformulated model. To quantify the statistics of the dual continnum model, we need to solve the coupled system for a large number of samples in the stochastic space. Thus the computation is prohibitively expensive. To exploit the advantages from the GMsFEM, we perform the iteration process in reduced GMsFE space to improve the computation efficiency. The proposed iterative method consisits of two stage, including an offline phase and an online phase. In offline stage, we compute local multiscale basis functions in each coarse grid region based on deterministic multiscale characteristics to construct offline spaces. In online phase, a fixed-point iteration method is employed to compute the solution of the reformulated model in the offline spaces. Additionally, convergence analysis is established under some structure conditions. Finally, we present two numerical tests to show the performance of our proposed method and validate the theoretical convergence results.

Key words. dual continuum model, iterative method, generalized multiscale finite element method, random inputs

MSC codes. 65N99, 65N30, 35R60

DOI. 10.1137/24M1695956

1. Introduction.

Fluid infiltration in porous media has a wide range of scientific and engineering applications [4, 26, 29, 39]. Typical examples include the flow of fluids through natural strata (e.g., groundwater and hydrocarbon reservoirs) and composite materials (e.g., membranes and catalysts) [7, 25, 27, 37, 40]. Specially, various applications related to natural strata typically require numerical simulations of domains containing discrete fissures, faults, and thin structures. The material properties within fractures can differ significantly from those in the background media, which can also contain highly heterogeneous and high-contrast regions. Due to complexity of natural phenomena, human lacking enough knowledge about the physical properties and measurement noise, model inputs often involve parameters or uncertainties. Uncertainties in fractured porous media typically involve variations in fracture morphology, dimensions, permeability, as well as properties of the background media and

*Received by the editors September 24, 2024; accepted for publication (in revised form) July 16, 2025; published electronically October 10, 2025.
https://doi.org/10.1137/24M1695956
Funding: This work was supported by National Key R&D Program of China grant 2021YFA1001300, National Natural Science Foundation of China grants 12288101, 12271150, 12471405, 12101217, 12331011, China Postdoctoral Science Foundation grant 2022M713875, and Natural Science Foundation of Hunan Province grant 2022JJ40113.
†School of Mathematics, Hunan University, Changsha, 410082 China (qli28@hnu.edu.cn).
‡Corresponding author. Department of Mathematics, National University of Defense Technology, Changsha, 410003 and School of Mathematics and Statistics, Hunan First Normal University, Changsha, 410205, China (hudalingling@126.com).
§School of Mathematics and Statistics, Wuhan University, Wuhan, 430072 and School of Mathematical Sciences, Laboratory of Mathematics and Applied Mathematics, Peking University, Beijing, 100871, China (pzhang@pku.edu.cn).

boundary conditions. These uncertainties significantly amplify computational complexity. Therefore, for such problems, we require a method capable of concurrently reducing computational costs while capturing multiscale information. The aim of this paper is to construct and analyze simplified models to address these types of problems.

Various techniques have been used for simulating flow in porous media with discrete fractures, including finite element scheme [2, 14, 15], finite volume scheme [5, 22], and hybrid scheme combining finite element method and finite volume method [21, 35]. Considering the existence of multiple scales and high-contrast within fractured media, the dual continuum model proposed by Barenblatt et al. [3] has been a standard approach to simulate these physical processes. The concept of this model originates from the idea of parallel interconnected dual systems distributed arbitrarily within the flow field. In the standard dual continuum model, mass transfer is coupled between two different-scale continua. One of these continua is typically called the fracture continuum, characterized by high permeability but a small volume. The other is known as the matrix continuum, which has low permeability but a larger volume. The coupling between the fracture and matrix continua is achieved using a transfer function that quantifies the mass transfer between them. Over the past 50 years, the dual-continuum model has been significantly extended and developed. Wu and Pruess expanded this model by introducing multiple interacting continua to capture the transient characteristics of flow between them [42]. Yan et al. further generalized this approach into a multicontinuum model capable of handling any number of continua and establishing arbitrary connections between them [44]. Due to the multiscale nature of these problems, various multiscale approaches have been proposed to couple multiple model equations for multiple continua [1, 8, 11, 12, 33, 36, 41]. These include the generalized multiscale finite element method (GMsFEM) [9, 13] and the constrained energy minimization generalized multiscale finite element method (CEM-GMsFEM) [10].

The generalized multiscale finite element method (GMsFEM) can be seen as an extension of the multiscale finite element method (MsFEM). The main idea of GMsFEM is to identify local dominant modes using spectral problems in snapshot spaces, which is crucial for capturing high-contrast channels and regions. This approach shares similarities with multiscale methods for multiple continua [11]. The concept of constructing local basis functions using spectral problems is also utilized in domain decomposition methods [20, 31]. The convergence of GMsFEM depends on the decay of eigenvalues in local spectral problems and the coarse mesh size [32]. When the multiscale approach is used to address model parameter heterogeneity, solving models with uncertain parameters remains a significant challenge. These uncertain parameters are typically parameterized by a few random variables, allowing the models to be described using parameterized partial differential equations (PPDEs) [43]. Several approaches have been proposed to tackle this problem, including variants of the model order reduction (MOR) method [6, 28, 38], ensemble method [23, 24, 30, 34], multimodes method [16, 17, 18, 45] and iterative method [19]. In 2021, Feng et al. proposed an iterative method for solving parameter-dependent convection-diffusion problems, building on ensemble and multimodal methods. The main idea is to reformulate a given parameter-dependent problem into one with parameter-independent convection and diffusion coefficients and a parameter-dependent (and solution-dependent) right-hand side. The solution is then computed using a fixed-point iteration algorithm. As a result, the convection and diffusion coefficients become independent of parameters and iterations, while the right-hand side remains dependent on parameters and iterations. This approach achieves computational savings by reusing a substantial portion of the computation for a given set of parameters.

Inspired by GMsFEM and iterative methods, this study aims to develop and analyze an efficient iterative method based on GMsFEM (Iter-GMsFEM) for solving parameter-dependent dual continuum models. The core concept involves reformulating the original parameter-dependent dual continuum model into a problem with deterministic multiscale permeability and parameter-dependent permeability and source functions. This reformulated problem can then be solved using a fixed-point iterative method [19]. As a result, the convection and diffusion coefficients become independent of parameters and iterations, while the right-hand side remains dependent on parameters and iterations. This allows us to utilize an efficient direct solver at each iteration to solve a linear system with multiple right-hand vectors. Traditional numerical methods such as finite volume methods, finite element methods, and their variants can be used to solve fine models on fine grids. However, for porous media with highly heterogeneous permeability fields and fractures, solving the model requires extremely fine meshes, which can be computationally expensive since the model needs to be solved on the fine grid at each iteration. Therefore, we introduce the GMsFEM method to reduce computational costs. GMsFEM includes two distinct stages: the offline and online stages. Similarly, our method also consists of two stages: offline and online. In the offline stage, we use GMsFEM to construct a multiscale basis functions space (offline space) based on deterministic multiscale permeability. In the online stage, we apply a fixed-point iteration method to solve the model in the multiscale basis functions space. Considering the shared features of the coefficient matrix by all parameter iterative functions, the inverse of the coefficient matrix can be reused, effectively reducing the complexity of repeated computations of discretized multiscale systems and leading to significant computational savings in the overall numerical method. Additionally, the convergence of Iter-GMsFEM is established with a linear dependency on the decay of eigenvalues in local spectral problems, mesh size, and number of iterations, and it is independent of contrast.

The paper is organized as follows. In section 2, we will present some preliminaries and notations for the parameter-dependent dual continuum model. Structure conditions and assumptions are stated to ensure the well-posedness of the variational problem and the convergence of the proposed method. The Iter-GMsFEM will be presented in section 3. Section 4 is to present the convergence analysis of the efficient iterative method. In section 5, some numerical examples for different dual continuum models are given to illustrate the proposed iterative method and confirm the theoretical analysis. Finally, some conclusions and comments are outlined in the last section.

2. Preliminaries and notations. In this section, we present some preliminaries and notations for the rest of paper. Let $(\mathcal{S}, \mathcal{B}, P)$ be a complete probability space, where $\mathcal{S}$ is the space of elementary events, $\mathcal{B}$ is a σ-algebra on $\mathcal{S}$, and P is the probability measure on $\mathcal{B}$. Let Ω denote a convex and bounded physical domain with Lipschitz continuous boundary $\partial\Omega$. $V := H_0^1(\Omega)$ is a Hilbert space defined on Ω with inner products $(\cdot,\cdot)_{\mathcal{V}}$. Its dual space is denoted by $V^* = H^{-1}(\Omega)$, which is the space of bounded linear functional on V. The Sobolev norm $\|\cdot\|_{H_0^1(\Omega)}$ is of the form

$$\|v\|_{H_0^1(\Omega)} = \left(\|v\|^2_{L^2(\Omega)} + \|\nabla v\|^2_{\boldsymbol{L}^2(\Omega)}\right)^{\frac{1}{2}}.$$

Here $\|\nabla v\|_{\boldsymbol{L}^2(\Omega)} := \||\nabla v|\|_{\boldsymbol{L}^2(\Omega)}$, and $|\nabla v|$ denotes the Euclidean norm of the 2-component vector-valued function ∇v; and for $\boldsymbol{v} = (v_1, v_2)$,$\|\nabla \boldsymbol{v}\|_{L^2(\Omega)} := \||\nabla \boldsymbol{v}|\|_{L^2(\Omega)}$, where $|\nabla \boldsymbol{v}|$ denotes the Frobenius norm of the 2×2 matrix $\nabla \boldsymbol{v}$. We recall that the Frobenius norm on $\mathbb{L}^2(\Omega)$ is defined by $|\boldsymbol{X}|^2 := \boldsymbol{X} \cdot \boldsymbol{X} = \mathrm{tr}(\boldsymbol{X}^{\mathrm{T}}\boldsymbol{X})$. To shorten

notation, we denote the space for $\boldsymbol{v}(\cdot,\boldsymbol{\xi}) = (v_1(\cdot,\boldsymbol{\xi}), v_2(\cdot,\boldsymbol{\xi}))$ by $\boldsymbol{V} = V \times V = H_0^1(\Omega) \times H_0^1(\Omega)$.

Let $v : \Omega \times \mathcal{S} \to \mathbb{R}$ represent a real-valued random field, i.e., real-valued random function defined in $\mathcal{S}$. For computation, the random field is usually approximated using a prescribed finite number of random variables, $\boldsymbol{\xi}(\omega) = \{\xi_1, \xi_2, \cdots, \xi_m\}$, i.e., $\boldsymbol{\xi}(\cdot) : \mathcal{S} \to D \subset \mathbb{R}^m$ $(m \geq 1)$. Thus, we use the random vector $\boldsymbol{\xi}(\omega)$ to characterize the stochastic property of the random field. Let ρ be the joint probability density function of $\boldsymbol{\xi}(\omega)$. We define the following tensor-product Hilbert space

$$\mathcal{H}_s(\Omega) := H^s(\Omega) \otimes L^2_\rho(D) = \Big\{ v : \Omega \times D \to \mathbb{R} | v(\cdot,\boldsymbol{\xi}) \in H^s(\Omega) \text{ and } \|v(\cdot,\boldsymbol{\xi})\|_{H^s(\Omega)} \in L^2_\rho(D), \forall \boldsymbol{\xi} \in D \Big\}.$$

For $\boldsymbol{v} = (v_1, v_2)$, we define the following tensor-product Hilbert space

$$\boldsymbol{V} := \boldsymbol{V} \otimes L^2_\rho(D) = \Big\{ \boldsymbol{v} : \Omega \times D \to \mathbb{R} | \boldsymbol{v}(\cdot,\boldsymbol{\xi}) \in \boldsymbol{V} \text{ and } \|\boldsymbol{v}(\cdot,\boldsymbol{\xi})\|_{\boldsymbol{V}} \in L^2_\rho(D), \forall \boldsymbol{\xi} \in D \Big\}$$

and equip it with the following norm

$$\|\boldsymbol{v}\|_{\boldsymbol{V}} := \left(\int_D \|\boldsymbol{v}\|_{\boldsymbol{V}} \rho \, \mathrm{d}\boldsymbol{\xi} \right)^{\frac{1}{2}}.$$

We consider the parameter-dependent dual-continuum model for the heterogeneous porous media in the steady state [3]. Using the concept of dual-continuum, we assume the porous media can be decomposed into two continua, namely fractures and background, which can also contain highly heterogeneous and high contrast regions. Let domain Ω be divided into the low permeability domain Ω_m^i and the high permeability domain Ω_f^i for continuum i. Furthermore, the domain Ω_f^i can be further decomposed into a union of individual channel domains $\Omega_{f,l}^i$. Therefore, Ω is expressed as

$$\Omega = \Omega_m^i \cup \Omega_f^i, \ \Omega_f^i = \cup_{l=1}^{n_f} \Omega_{f,l}^i,$$

where n_f represents the count of highly conductive channels. In addition, the model accounts for the transfer between these two continua using an exchange term. Thus, the mass balance equations describing this coupled dual continuum model read

$$\begin{cases} -\operatorname{div}(\kappa_1(x,\boldsymbol{\xi})\nabla p_1(x,\boldsymbol{\xi})) + \sigma(x)(p_1(x,\boldsymbol{\xi}) - p_2(x,\boldsymbol{\xi})) = f_1(x,\boldsymbol{\xi}), \\ -\operatorname{div}(\kappa_2(x,\boldsymbol{\xi})\nabla p_2(x,\boldsymbol{\xi})) - \sigma(x)(p_1(x,\boldsymbol{\xi}) - p_2(x,\boldsymbol{\xi})) = f_2(x,\boldsymbol{\xi}), \end{cases} \tag{2.1}$$

in $\Omega \times D$. Here, the Dirichlet boundary condition is set as $p_i(x,\boldsymbol{\xi}) = g_i(x,\boldsymbol{\xi})$ on $\partial\Omega \times D$ for $i = 1, 2.p_i(x,\boldsymbol{\xi})$ denotes the pressure and $f_i(x,\boldsymbol{\xi})$ is the source function corresponding to the i-th continuum for $i = 1, 2$, and $\sigma(x)$ is a transfer function. The coefficient $\kappa_i(x,\boldsymbol{\xi})$ represent random permeability and is defined as

$$\kappa_i(x,\boldsymbol{\xi}) = \begin{cases} \kappa_i^m(x,\boldsymbol{\xi}), x \in D_m^i, \\ \kappa_{l,i}^f(x,\boldsymbol{\xi}), x \in D_{f,l}^i \end{cases}, \ i = 1, 2, \ l = 1, \ldots, n_f,$$

where $\kappa_{l,i}^f$ are the permeability on the l-th channel for the continuum i in subdomain $D_{f,l}^i$; κ_i^m are the permeability in subdomain D_m^i. It is noteworthy that p_i, κ_i, and f_i are all contingent on the parameter vector $\boldsymbol{\xi}$, while σ remains independent of $\boldsymbol{\xi}$.

The variational problem for the model (2.1) reads the following: find $\boldsymbol{p} = (p_1, p_2) \in \boldsymbol{V}$ such that

$$a(\boldsymbol{p}, \boldsymbol{v}; \boldsymbol{\xi}) + q(\boldsymbol{p}, \boldsymbol{v}) = b(\boldsymbol{v}; \boldsymbol{\xi}), \tag{2.2}$$

for all $\boldsymbol{v} = (v_1, v_2) \in \boldsymbol{V}$. Here $b(\boldsymbol{v}; \boldsymbol{\xi}) \in \boldsymbol{V}^*$ and $a(\boldsymbol{p}, \boldsymbol{v}; \boldsymbol{\xi}) : \boldsymbol{V} \times \boldsymbol{V} \to \mathbb{R}$ depend on a parameter $\boldsymbol{\xi}$ for given $\boldsymbol{\xi}$, while $q(\boldsymbol{p}, \boldsymbol{v}) : \boldsymbol{V} \times \boldsymbol{V} \to \mathbb{R}$ is independent of a parameter $\boldsymbol{\xi}$. Moreover, the linear form is defined as

$$b(\boldsymbol{v}; \boldsymbol{\xi}) = \sum_i b_i(v_i; \boldsymbol{\xi}) = \sum_i \left(\int_\Omega f_i(x, \boldsymbol{\xi}) v_i(x, \boldsymbol{\xi})\, dx + \int_{\partial\Omega} \kappa_i(x) \nabla g_i(x) \nabla v_i(x, \boldsymbol{\xi})\, ds \right),$$

and the bilinear forms are defined as

$$\begin{aligned}
a_i(p_i, v_i; \boldsymbol{\xi}) &= \int_{D_m^i} \kappa_i^m(x, \boldsymbol{\xi}) \nabla p_i(x, \boldsymbol{\xi}) \cdot \nabla v_i(x; \boldsymbol{\xi})\, dx \\
&\quad + \sum_l \int_{D_{f,l}^i} \kappa_{l,i}^f(x, \boldsymbol{\xi}) \nabla p_i(x, \boldsymbol{\xi}) \cdot \nabla v_i(x; \boldsymbol{\xi})\, dx \\
&= \int_\Omega \kappa_i(x, \boldsymbol{\xi}) \nabla p_i(x, \boldsymbol{\xi}) \cdot \nabla v_i(x; \boldsymbol{\xi})\, dx, \\
a(\boldsymbol{p}, \boldsymbol{v}; \boldsymbol{\xi}) &= \sum_i a_i(p_i, v_i; \boldsymbol{\xi}), \\
Q(p_i, v_i) &= \int_\Omega \sigma(x) p_i(x, \boldsymbol{\xi}) v_i(x; \boldsymbol{\xi})\, dx, \\
q(\boldsymbol{p}, \boldsymbol{v}) &= \sum_i \sum_l Q(p_i, v_i) - Q(p_l, v_i).
\end{aligned}$$

Given parameter $\boldsymbol{\xi}$, we define a norm $\|\cdot\|_{a_Q}$ on the space $\boldsymbol{V}$ as

$$\|\boldsymbol{v}\|_{a_Q}^2 := a_Q(\boldsymbol{v}, \boldsymbol{v}; \boldsymbol{\xi}) = a(\boldsymbol{v}, \boldsymbol{v}; \boldsymbol{\xi}) + q(\boldsymbol{v}, \boldsymbol{v}),$$

and $a_Q(\cdot, \cdot; \boldsymbol{\xi})$ satisfies the following assumption [36].

Assumption 2.1.

(i) *Bilinearity*: $a_Q(\boldsymbol{v}, \boldsymbol{v}; \boldsymbol{\xi})$ is bilinear mapping on $\boldsymbol{V} \times \boldsymbol{V}$.

(ii) *Boundedness*: Suppose there exist positive constants $\underline{\kappa}$, $\overline{\kappa}$, and $\overline{\sigma}$ such that $\underline{\kappa} \le \kappa_i(x, \boldsymbol{\xi}) \le \overline{\kappa}$ for $i = 1, 2$ and $|\sigma(x)| \le \overline{\sigma}$. Then, there exists a $\boldsymbol{\xi}$-independent constant D_1 such that

$$a_Q(\boldsymbol{v}, \boldsymbol{w}; \boldsymbol{\xi}) \le D_1 \|\boldsymbol{v}\|_{a_Q} \|\boldsymbol{w}\|_{a_Q}, \ \forall \boldsymbol{v}, \boldsymbol{w} \in \boldsymbol{V}.$$

(iii) *Coercivity*: If $(1 + \frac{2\overline{\sigma} C_p^2}{\underline{\kappa}})^{-1} \ge \frac{2\overline{\sigma} C_p}{\sqrt{\underline{\kappa}}}$ with C_p being Poincaré constant, there is a $\boldsymbol{\xi}$-independent constant D_1 such that

$$a_Q(\boldsymbol{v}, \boldsymbol{v}; \boldsymbol{\xi}) \ge D_2 \|\boldsymbol{v}\|_{a_Q}^2, \ \forall \boldsymbol{v} \in \boldsymbol{V}.$$

C_p is the Poincaré constant depending on the dimension of the functional space and the domain, i.e., $C_p = C_p(n, \Omega)$.

Under the above assumptions, the dual-continuum model is well-posed.

3. The Iter-GMsFEM framework. In this section, we introduce an Iter-GMsFEM to solve problem (2.1). The main idea of the framework is to reformulate original problem (2.2) into another problem with parameter-independent multiscale permeability coefficients and exchange term and a parameter-dependent (and solution-dependent) right-hand side. We then employ a fixed-point iteration scheme to compute the solution of this reformulated problem. Due to the presence of heterogeneous coefficients, solving the reformulated problem on a fine grid using standard FEM methods becomes prohibitively expensive. To this end, we utilize the GMsFEM to improve the computation efficiency. The new method aims at achieving computational efficiency and effectively addressing the multiscale characteristics of the problem. In the following subsections, we present the details of the iterative method.

3.1. The iterative method. We firstly assume the random permeability $\kappa_i(x, \boldsymbol{\xi})$, for $i = 1, 2$, can be decomposed into two parts, i.e.,

$$\kappa_i(x, \boldsymbol{\xi}) := \kappa_i^0(x) + \kappa_i^1(x, \boldsymbol{\xi}),$$

where $\kappa_i^0(x)$ is the deterministic coefficients with multiscale characteristic, and $\kappa_i^1(x, \boldsymbol{\xi})$ is the random fluctuation. The bilinear form $a(\boldsymbol{p}, \boldsymbol{v}; \boldsymbol{\xi})$ can be redefined as

$$a(\boldsymbol{p}, \boldsymbol{v}; \boldsymbol{\xi}) = a^0(\boldsymbol{p}, \boldsymbol{v}) + a^1(\boldsymbol{p}, \boldsymbol{v}; \boldsymbol{\xi}),$$

where

$$\begin{aligned} a_i^0(p_i, v_i) &= \int_\Omega \kappa_i^0(x) \nabla p_i(x, \boldsymbol{\xi}) \cdot \nabla v_i(x)\, dx, \\ a^0(\boldsymbol{p}, \boldsymbol{v}) &= \sum_i a_i^0(p_i, v_i), \\ a_i^1(p_i, v_i; \boldsymbol{\xi}) &= \int_\Omega \kappa_i^1(x, \boldsymbol{\xi}) \nabla p_i(x, \boldsymbol{\xi}) \cdot \nabla v_i(x)\, dx, \\ a^1(\boldsymbol{p}, \boldsymbol{v}; \boldsymbol{\xi}) &= \sum_i a_i^1(p_i, v_i; \boldsymbol{\xi}). \end{aligned}$$

Here, $a^0(\cdot, \cdot) : \boldsymbol{V} \times \boldsymbol{V} \to \mathbb{R}$ is a $\boldsymbol{\xi}$-independent bilinear form, and $a^1(\cdot, \cdot : \boldsymbol{\xi}) : \boldsymbol{V} \times \boldsymbol{V} \to \mathbb{R}$ is a $\boldsymbol{\xi}$-dependent bilinear form. Thus, the weak formulation (2.2) can be rewritten as

$$a^0(\boldsymbol{p}, \boldsymbol{v}) + q(\boldsymbol{p}, \boldsymbol{v}) = b(\boldsymbol{v}; \boldsymbol{\xi}) - a^1(\boldsymbol{p}, \boldsymbol{v}; \boldsymbol{\xi}). \tag{3.1}$$

We now state the iterative algorithm for solving (2.1).

To ensure the convergence of the Algorithm 3.1 and efficient computation, we must provide the specific condition between $\kappa_i^0(x)$ and $\kappa_i^1(x, \boldsymbol{\xi})$, for $i = 1, 2$. Specifically, it is described as

Algorithm 3.1. An iterative algorithm in variational setting.

Step 1: For each $\boldsymbol{\xi} \in D$, find $\boldsymbol{P}_0 = \boldsymbol{P}_0(\boldsymbol{\xi}) \in \boldsymbol{V}$ by solving the following problem

$$a^0(\boldsymbol{P}_0, \boldsymbol{v}) + q(\boldsymbol{P}_0, \boldsymbol{v}) = b(\boldsymbol{v}; \boldsymbol{\xi}),\ \forall \boldsymbol{v} \in \boldsymbol{V}. \tag{3.2}$$

Step 2: For each $\boldsymbol{\xi} \in D$, determine $\{P_n = P_n(\boldsymbol{\xi})\}_{n \geq 1} \subset \boldsymbol{V}$ recursively by solving the problem

$$a^0(\boldsymbol{P}_n, \boldsymbol{v}) + q(\boldsymbol{P}_n, \boldsymbol{v}) = b(\boldsymbol{v}; \boldsymbol{\xi}) - a^1(\boldsymbol{P}_{n-1}, \boldsymbol{v}; \boldsymbol{\xi}),\ \forall \boldsymbol{v} \in \boldsymbol{V}. \tag{3.3}$$

$$\underline{\kappa^0} - 2\overline{\sigma} C_p^2 \geq \overline{\kappa^1}, \tag{3.4}$$

where

$$\underline{\kappa^0} \leq \kappa_i^0(x),\ \overline{\kappa^1} \geq \kappa_i^1(x,\boldsymbol{\xi}),\ \forall x \in \Omega,\ \forall \boldsymbol{\xi} \in D,\ i = 1,2.$$

This condition is highly dependent on the problem and can be quite intricate. The detailed condition will be presented and proven in section 4.

Remark 3.1. The primary advantage of Algorithm 3.1 lies in the fact that the left-hand side expressions in (3.2) and (3.3) are identical and independent of the parameter $\boldsymbol{\xi}$. For a large number of random parameters, this characteristic allows to design fast solvers for computing solutions in both steps of Algorithm 3.1.

3.2. The approximation based on FEM. Before giving the framework of FE approximation for dual continuum model, we firstly set the scene of the numerical discretization, as demonstrated in Figure 1. We assume that the spatial domain Ω is partitioned uniformly by a coarse mesh $\mathcal{T}^H$. The partition $\mathcal{T}^H$ is called a coarse grid, and a generic element K in the partition $\mathcal{T}^H$ is called a coarse element. $H > 0$ is called as coarse mesh size. Moreover, the fine-grid partition will be denoted by $\mathcal{T}^h$, which is obtained by refining the coarse mesh $\mathcal{T}^H$. Similarly, $h > 0$ is the fine mesh size. N_h denotes the number of elements in $\mathcal{T}^H$. We denote by$\{x_j\}_{j=1}^{N_c}$ the vertices of the coarse grid $\mathcal{T}^H$, where N_c represents the total number of coarse nodes. The neighborhood ω_j of the node x_j consists of all the coarse mesh elements, i.e.,

$$\omega_j = \cup\{K_i \in \mathcal{T}^H | x_j \in \overline{K_i}\}.$$

The overlap constant C_{ov} is defined by

$$C_{\text{ov}} := \max_{K \in \mathcal{T}^H} \#\{x_j : K \subset \omega_j \text{ for } j = 1,2,\ldots,N_c\}. \tag{3.5}$$

Let $\boldsymbol{V}^h = V^h \times V^h$ be the finite element space on fine grid and $\boldsymbol{V}_0^h \subset \boldsymbol{V}^h$ with vanish boundary values. The Galerkin formulation of (2.2) reads the following: given $\boldsymbol{\xi} \in D$, find $\boldsymbol{p}^h = (p_1^h, p_2^h) \in \boldsymbol{V}^h$ such that

$$a(\boldsymbol{p}^h, \boldsymbol{v}; \boldsymbol{\xi}) + q(\boldsymbol{p}^h, \boldsymbol{v}) = b(\boldsymbol{v}; \boldsymbol{\xi}), \tag{3.6}$$

for all $\boldsymbol{v} = (v_1^h, v_2^h) \in \boldsymbol{V}^h$.

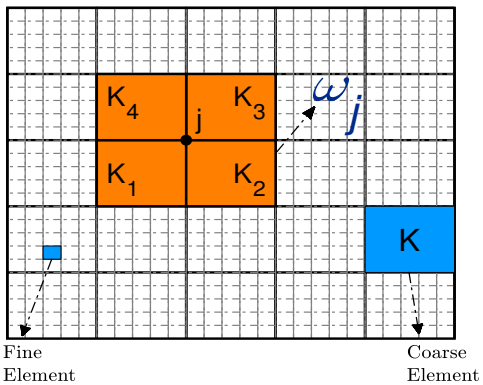

FIG. 1. *Illustration of discretization configuration.*

Algorithm 3.2. An iterative algorithm in discrete setting.

step 1: For each $\boldsymbol{\xi} \in D$, find $\boldsymbol{U}_0^h = \boldsymbol{P}_0^h(\boldsymbol{\xi}) \in \boldsymbol{V}_0^h$ by solving the following problem:

$$a^0(\boldsymbol{P}_0^h, \boldsymbol{v}) + q(\boldsymbol{P}_0^h, \boldsymbol{v}) = b(\boldsymbol{v}; \boldsymbol{\xi}),\ \forall \boldsymbol{v} \in \boldsymbol{V}_0^h. \tag{3.8}$$

step 2: For each $\boldsymbol{\xi} \in D$, recursively determine $\{\boldsymbol{P}_n^h = \boldsymbol{U}_n^h(\boldsymbol{\xi})\}_{n\geq 1} \subset \boldsymbol{V}_0^h$ by solving the following problem:

$$a^0(\boldsymbol{P}_n^h, \boldsymbol{v}) + q(\boldsymbol{P}_n^h, \boldsymbol{v}) = b(\boldsymbol{v}; \boldsymbol{\xi}) - a^1(\boldsymbol{P}_{n-1}^h, \boldsymbol{v}; \boldsymbol{\xi}),\ \forall \boldsymbol{v} \in \boldsymbol{V}_0^h. \tag{3.9}$$

Using the definition of a^0 and a^1, we can rewrite (3.6) as follows:

$$a_0(\boldsymbol{p}^h, \boldsymbol{v}) + q(\boldsymbol{p}^h, \boldsymbol{v}) = b(\boldsymbol{v}; \boldsymbol{\xi}) - a_1(\boldsymbol{p}^h, \boldsymbol{v}; \boldsymbol{\xi}). \tag{3.7}$$

We can then can easily formulate the discrete version of Algorithm 3.1 for computing the solution of equation (3.6) below.

When the model with multiscale feature is considered, both the degrees of freedom in the finite element approximation and the number of iterations must be sufficiently large to achieve accurate results. Furthermore, the model involving the influence of uncertainty, the Algorithm 3.2 are needed to be implemented repeatedly. This will lead to significant computational cost and storage. To take account of this issue, we use GMsFEM as a local model reduction method to efficiently solve the parameter-dependent dual-continuum model.

3.3. The approximation based on GMsFEM. In this subsection, we will introduce the framework of the Iter-GMsFEM to solve the parameter-dependent dual continuum model with multiscale feature. We will outline the construction procedure of the multiscale finite element space of GMsFEM. The GMsFEM uses the coarse grid $\mathcal{T}^H$ and constructs a local reduced-order model for each coarse block. Firstly, for each coarse region ω_j, we find the eigenvalue $\lambda_k^{(j)} \in \mathbb{R}$ and the eigenfunction $\boldsymbol{\psi}_k^{(j)} = (\psi_{k,1}^{(j)}, \psi_{k,2}^{(j)}) \in \boldsymbol{V}(\omega_j)$, where $\boldsymbol{V}(\omega_j) = V(\omega_j) \times V(\omega_j)$ such that

$$\begin{cases} -\operatorname{div}(\kappa_1^0 \nabla \psi_{k,1}^{(j)}) + \sigma(\psi_{k,1}^{(j)} - \psi_{k,2}^{(j)}) = \lambda_k^{(j)} \widetilde{\kappa}_1^0 \psi_{k,1}^{(j)} & \text{in } \omega_j, \\ \kappa_1^0 \cdot \nabla \psi_{k,1}^{(j)} \cdot n = 0 & \text{on } \partial\omega_j, \\ -\operatorname{div}(\kappa_2^0 \nabla \psi_{k,2}^{(j)}) + \sigma(\psi_{k,2}^{(j)} - \psi_{k,1}^{(j)}) = \lambda_k^{(j)} \widetilde{\kappa}_2^0 \psi_{k,2}^{(j)} & \text{in } \omega_j, \\ \kappa_2^0 \cdot \nabla \psi_{k,2}^{(j)} \cdot n = 0 & \text{on } \partial\omega_j. \end{cases} \tag{3.10}$$

Here $\widetilde{\kappa}_i^0 = \kappa_i^0 \sum_{j=1}^{N_C} H^2 |\nabla \chi_{j,i}|^2$ for $i = 1, 2$ and $\{\chi_{j,i}\}$ is a set of bilinear partition of unity functions for the coarse grid partition of the domain Ω.

We choose the M_j smallest eigenvalues and the corresponding eigenvectors of the eigenvalue problem (3.10). Then we use these eigenfunctions to construct the local spectral offline space.

$$\boldsymbol{V}_{\text{off}}^{j,M_j} = \operatorname{span}\left\{ \boldsymbol{\psi}_k^{(j)} :\ 1 \leq k \leq M_j \right\},$$

where $\boldsymbol{\psi}_1^{(j)} = 1$. The choice of the truncation number $M_j \in \mathbb{N}_+$ has to be determined by the eigenvalue decay rate or the presence of spectral gap. Furthermore, we can define the k-th multiscale basis function on the coarse neighborhood ω_j by

Algorithm 3.3. Iterative method.

step 1: For each $\boldsymbol{\xi} \in D$, find $\boldsymbol{P}_0^{\mathrm{ms}} = \boldsymbol{P}_0^{\mathrm{ms}}(\boldsymbol{\xi}) \in \boldsymbol{V}_{\mathrm{ms}}$ solve the following problem

$$a^0(\boldsymbol{P}_0^{\mathrm{ms}}, \boldsymbol{v}) + \sigma(\boldsymbol{P}_0^{\mathrm{ms}}, \boldsymbol{v}) = b(\boldsymbol{v}; \boldsymbol{\xi}), \ \forall \boldsymbol{v} \in \boldsymbol{V}_{\mathrm{ms}}. \tag{3.11}$$

step 2: For each $\boldsymbol{\xi} \in D$, recursively determine $\{\boldsymbol{P}_n^{\mathrm{ms}} = \boldsymbol{P}_n^{\mathrm{ms}}(\boldsymbol{\xi})\}_{n\geq 1} \subset \boldsymbol{V}_{\mathrm{ms}}$ by solving the following problem

$$a^0(\boldsymbol{P}_n^{\mathrm{ms}}, \boldsymbol{v}) + \sigma(\boldsymbol{P}_n^{\mathrm{ms}}, \boldsymbol{v}) = b(\boldsymbol{v}; \boldsymbol{\xi}) - a^1(\boldsymbol{P}_{n-1}^{\mathrm{ms}}, \boldsymbol{v}; \boldsymbol{\xi}), \ \forall \boldsymbol{v} \in \boldsymbol{V}_{\mathrm{ms}}. \tag{3.12}$$

$$\boldsymbol{\psi}_{j,k} = \left(\chi_{j,1}\psi_{k,1}^{(j)}, \chi_{j,2}\psi_{k,2}^{(j)}\right), \ 1 \leq k \leq M_j.$$

We introduce the local reduced space on the coarse neighborhood ω_j

$$\boldsymbol{V}_{\mathrm{ms}}(\omega_j) = \mathrm{span}\left\{\boldsymbol{\psi}_{j,k}, \ 1 \leq k \leq M_j\right\}.$$

Finally, the multiscale finite element space is obtained as

$$\boldsymbol{V}_{\mathrm{ms}} := \mathrm{span}\left\{\boldsymbol{\psi}_\ell : 1 \leq \ell \leq M\right\} = \mathrm{span}\left\{\boldsymbol{\psi}_{j,k}, \ 1 \leq j \leq N_c, \ 1 \leq k \leq M_j\right\},$$

where $M = \sum_{j=1}^{N_c} M_j$ is the total number of eigenvectors for snapshots. Let Ψ_ℓ be the coefficient vector associated with the basis functions of the fine space $\boldsymbol{V}_0^h$. We can create the offline matrix R to store these the coefficient vectors, i.e.,

$$R^T = [\Psi_1, \Psi_2, \ldots, \Psi_M].$$

Then the Iter-GMsFEM is described in Algorithm 3.3.

3.4. Matrix formulation. In the previous section, we have outlined the construction of the multiscale finite element space (offline space) $\boldsymbol{V}_{\mathrm{ms}}$ and the matrix R. Based on these multiscale basis functions, we need to assemble them into an algebraic system for computation.

In the context of finite element discretization, we suppose that $\boldsymbol{P}_n^h$ have the following formulations

$$P_{n,i}^h(x, \boldsymbol{\xi}) = \sum_\ell c_{\ell,i}^{n,h}(\boldsymbol{\xi})\, \psi_{\ell,i}^h(x), \ i = 1, 2, \tag{3.13}$$

where $\psi_{\ell,i}^h$, for $1 \leq \ell \leq N_h$, $i = 1, 2$, are the finite element basis functions. Then, the matrix representation of (3.8) and (3.9) can be expressed as

$$\mathbf{A}_0 \boldsymbol{c}^{n,h}(\boldsymbol{\xi}) + \mathbf{B}\boldsymbol{c}^{n,h}(\boldsymbol{\xi}) = \begin{cases} \mathbf{b}(\boldsymbol{\xi}), & n = 0, \\ \mathbf{b}(\boldsymbol{\xi}) - \mathbf{A}_1(\boldsymbol{\xi})\boldsymbol{c}^{n-1,h}(\boldsymbol{\xi}), & n \geq 1. \end{cases}$$

Here, parameter-independent matrices $\mathbf{A}_0$ and $\mathbf{B}$ are defined as

$$\mathbf{A}_0 = \begin{bmatrix} A_0^1 & \\ & A_0^2 \end{bmatrix}, \ \mathbf{B} = \begin{bmatrix} B & -B \\ -B & B \end{bmatrix},$$

where

$$(A_0^l)_{ij} = a^0(\psi_{i,l}^h, \psi_{j,l}^h), \quad (B)_{ij} = q(\psi_{i,l}^h, \psi_{j,l}^h), \ l = 1, 2.$$

Additionally, matrix $\mathbf{A}_1(\boldsymbol{\xi})$ and vectors $\mathbf{b}(\boldsymbol{\xi})$ and $\boldsymbol{c}^{n,h}(\boldsymbol{\xi})$ are parameter-dependent and are defined as

$$\mathbf{A}_1(\boldsymbol{\xi}) = \begin{bmatrix} A_1^1(\boldsymbol{\xi}) & \\ & A_1^2(\boldsymbol{\xi}) \end{bmatrix},\ \mathbf{b}(\boldsymbol{\xi}) = \begin{bmatrix} b_1(\boldsymbol{\xi}) \\ b_2(\boldsymbol{\xi}) \end{bmatrix},\ \boldsymbol{c}^{n,h}(\boldsymbol{\xi}) = \begin{bmatrix} \boldsymbol{c}_1^{n,h}(\boldsymbol{\xi}) \\ \boldsymbol{c}_2^{n,h}(\boldsymbol{\xi}) \end{bmatrix},$$

where

$$(A_1^l(\boldsymbol{\xi}))_{ij} = a^1(\psi_{i,l}^h, \psi_{j,l}^h; \boldsymbol{\xi}), \quad (b_l(\boldsymbol{\xi}))_i = b(\psi_{i,l}^h; \boldsymbol{\xi}), \quad (\boldsymbol{c}_l^{n,h}(\boldsymbol{\xi}))_i = c_{l,i}^{n,h}(\boldsymbol{\xi}),\ l = 1, 2.$$

In the context of multiscale finite element discretization, we suppose that $\boldsymbol{P}_n^{\mathrm{ms}}$ have the following formulations

$$P_{n,i}^{\mathrm{ms}}(x, \boldsymbol{\xi}) = \sum_{\ell} c_{\ell,i}^{n,\mathrm{ms}}(\boldsymbol{\xi})\, \psi_{\ell,i}(x),\ i = 1, 2.$$

Then, (3.11) and (3.12) can be rewritten in the following matrix form

$$\mathbf{A}_0^{\mathrm{ms}} \boldsymbol{c}^{n,\mathrm{ms}}(\boldsymbol{\xi}) + \mathbf{B}^{\mathrm{ms}} \boldsymbol{c}^{n,\mathrm{ms}}(\boldsymbol{\xi}) = \begin{cases} \mathbf{b}^{\mathrm{ms}}(\boldsymbol{\xi}), & n = 0, \\ \mathbf{b}^{\mathrm{ms}}(\boldsymbol{\xi}) - \mathbf{A}_1^{\mathrm{ms}}(\boldsymbol{\xi}) \boldsymbol{c}^{n-1,\mathrm{ms}}(\boldsymbol{\xi}), & n \geq 1, \end{cases} \tag{3.14}$$

where $\boldsymbol{c}^{n,\mathrm{ms}}(\boldsymbol{\xi})$ is represented as

$$\boldsymbol{c}^{n,\mathrm{ms}}(\boldsymbol{\xi}) = (\boldsymbol{c}_1^{n,\mathrm{ms}}(\boldsymbol{\xi}), \boldsymbol{c}_2^{n,\mathrm{ms}}(\boldsymbol{\xi}))^T,\ \text{with } (\boldsymbol{c}_l^{n,\mathrm{ms}}(\boldsymbol{\xi}))_i = c_{i,l}^{n,\mathrm{ms}}(\boldsymbol{\xi}),\ l = 1, 2.$$

According to matrix R obtained in the offline phase, we construct the reduced matrices $\mathbf{A}_0^{\mathrm{ms}}$, $\mathbf{B}^{\mathrm{ms}}$, $\mathbf{A}_1^{\mathrm{ms}}(\boldsymbol{\xi})$, and vector $\mathbf{b}^{\mathrm{ms}}(\boldsymbol{\xi})$ defined as follows

$$\begin{aligned} &\mathbf{A}_0^{\mathrm{ms}} = R\mathbf{A}_0 R^T, && \mathbf{B}^{\mathrm{ms}} = R\mathbf{B}R^T, \\ &\mathbf{A}_1^{\mathrm{ms}}(\boldsymbol{\xi}) = R\mathbf{A}_1(\boldsymbol{\xi})R^T, && \mathbf{b}^{\mathrm{ms}}(\boldsymbol{\xi}) = R\mathbf{b}(\boldsymbol{\xi}). \end{aligned}$$

Algorithm 3.4 describes the Iter-GMsFEM in the matrix formulation.

Remark 3.2. We note that the matrices $\mathbf{A}_0$, $\mathbf{B}$, R, and $\mathbf{A}_0^{\mathrm{ms}}$ and $\mathbf{B}_0^{\mathrm{ms}}$ are only computed once in our method. If all the diffusion coefficients $\kappa_i^1(x, \boldsymbol{\xi})$ and the source terms $f_i(x, \boldsymbol{\xi})$ are affine with respect to the parameter $\boldsymbol{\xi}$, i.e.,

$$\kappa_i^1(x, \boldsymbol{\xi}) = \sum_{j=1}^{m_k} \alpha_j(\boldsymbol{\xi}) \kappa_{j,i}^1(x),\ f_i(x, \boldsymbol{\xi}) = \sum_{j=1}^{m_f} \beta_j(\boldsymbol{\xi}) f_{j,i}(x),$$

the stiffness matrix $\mathbf{A}_1^{\mathrm{ms}}(\boldsymbol{\xi})$ and the load vector $\mathbf{b}^{\mathrm{ms}}(\boldsymbol{\xi})$ are the summations of m_k reduced matrices and m_f reduced vectors (parameter-independent) in the online phase, not involving the reconstruction and calculation of the full order matrices and load vectors.

Remark 3.3. We note that the iteration will be stopped when the iterative error falls below the iteration threshold. In the proposed iterative method, since the GMsFEM error exceeds the iteration threshold, the iteration can be terminated early.

Remark 3.4. Since the proposed Iter-GMsFEM method is developed within the GMsFEM framework, the accuracy of its solutions is closely related to the number of local basis functions used in constructing the multiscale space. Specifically, when fewer local basis functions are employed, the error between the Iter-GMsFEM solutions and the reference solutions tends to be larger, resulting in fewer required iterations and earlier termination of the iterative process. Conversely, when a larger number of basis functions are utilized, the error between the Iter-GMsFEM solutions and the reference solutions decreases, necessitating more iterations and leading to a later convergence of the iterative procedure.

Algorithm 3.4. Detailed procedure of Iter-GMsFEM.

Input: The dual-continuum model (2.1), maximum number of iteration N_{iter}, and the error tolerance ϵ.
Output: The Iter-GMsFEM solution $\boldsymbol{P}^{\text{Iter}-\text{GMs}}(\boldsymbol{\xi})$.
Offline phase: only perform once
1: Compute full order matrices $\mathbf{A}_0$ and $\mathbf{B}$ independent of $\boldsymbol{\xi}$;
2: Calculate projective matrix R by GMsFEM;
3: Assemble the reduced stiffness matrix $\mathbf{A}_0^{\text{ms}}$ and reduced mass matrix $\mathbf{B}^{\text{ms}}$;
4: Calculate and store the matrix $\mathbf{A}^{'} = (\mathbf{A}_0^{\text{ms}} + \mathbf{B}^{\text{ms}})^{-1}$;
Online phase: for arbitrary sample $\boldsymbol{\xi} \in \Omega$
1: With $n = 0$, solve (3.14) to get the solution coefficient $\boldsymbol{c}^{0,\text{ms}}(\boldsymbol{\xi})$;
2: Renew the load vector $\mathbf{b}^{\text{ms}}(\boldsymbol{\xi})$ and the matrix $\mathbf{A}_1^{\text{ms}}(\boldsymbol{\xi})$;
3: Calculate the coefficient $\boldsymbol{c}^{n,\text{ms}}(\boldsymbol{\xi})$ by (3.14);
4: Compute the error $\epsilon_n = \|\boldsymbol{c}^{n,\text{ms}}(\boldsymbol{\xi}) - \boldsymbol{c}^{n-1,\text{ms}}(\boldsymbol{\xi})\|_\infty$;
5: **while** $n < N_{\text{iter}}$ or $\epsilon_n \geq \epsilon$ **do**
6: $\quad n \to n+1$;
7: $\quad$ Return to the step 3–4 in the online phase;
8: **end while**
9: Obtain the Iter-GMsFEM solution $\boldsymbol{P}^{\text{Iter}-\text{GMs}}(\boldsymbol{\xi})$ by matrix R.

4. Convergence analysis. In this section, we will give the convergence analysis of our proposed Iter-GMsFEM in the sense of a_Q norm. Firstly, we give an error estimate for the deterministic dual-continuum model. Secondly, an error estimate for the iterative method are provide. Based on an error estimate for the deterministic dual-continuum model, we derive an error estimate of between the iterative method and Iter-GMsFEM. Finally, the global error estimate are obtained by the triangular inequality based on last two error estimates.

For the deterministic case, we are inspired by the work of Li [32] to drive the error estimate. To start with, we define local functional space and related norms on ω_j. Let $\boldsymbol{L}^2_{\widetilde{\kappa}}(\omega_j)$ be Hilbert spaces with their inner products and norms defined by

$$(\boldsymbol{v}_1, \boldsymbol{v}_2)_j := \sum_i (v_{1,i}, v_{2,i})_j^i, \quad (v_{1,i}, v_{2,i})_j^i := \int_{\omega_j} \widetilde{\kappa}_i v_{1,i} \cdot v_{2,i}\, dx,$$
$$\|\boldsymbol{v}_1\|^2_{\boldsymbol{L}^2_{\widetilde{\kappa}}(\omega_j)} := (\boldsymbol{v}_1, \boldsymbol{v}_1)_j, \qquad \forall \boldsymbol{v}_1, \boldsymbol{v}_2 \in \boldsymbol{L}^2_{\widetilde{\kappa}}(\omega_j),$$

respectively. We also define the a_Q norm as follows

$$a_Q^{(j)}(\boldsymbol{v}_1, \boldsymbol{v}_2) := \int_{\omega_j} \kappa_1(x) v_{1,1} \cdot v_{2,1} + \sigma(x)(v_{1,1} - v_{1,2}) v_{2,1}\ \mathrm{d}x + \int_{\omega_j} \kappa_2(x) v_{1,2} \cdot v_{2,2} + \sigma(x)(v_{1,2} - v_{1,1}) v_{2,2}\ \mathrm{d}x,$$
$$\|\boldsymbol{v}_1\|^2_{a_Q(\omega_j)} := a_Q^{(j)}(\boldsymbol{v}_1, \boldsymbol{v}_1).$$

Furthermore, we introduce the following weighted Sobolev space

$$\boldsymbol{L}^2_{\widetilde{\kappa}^{-1}}(\omega_j) := \left\{ \boldsymbol{v} : \|\boldsymbol{v}\|^2_{L^2_{\widetilde{\kappa}^{-1}}(\omega_j)} := \int_{\omega_j} \widetilde{\kappa}_1^{-1} v_1^2\ \mathrm{d}x + \int_{\omega_j} \widetilde{\kappa}_2^{-1} v_2^2\ \mathrm{d}x < \infty \right\}.$$

Similarly, we can define the weighted Sobolev space $\boldsymbol{L}^2_{\widetilde{\kappa}^{-1}}(\Omega)$ and its associated norm $\|\cdot\|^2_{L^2_{\widetilde{\kappa}^{-1}}(\Omega)}$ on the whole domain.

The solution $\boldsymbol{p}^{(j)} = (p_1^{(j)}, p_2^{(j)}) = (p_1|_{\omega_j}, p_2|_{\omega_j})$ satisfies the equation

$$\begin{cases} -\operatorname{div}(\kappa_1 \nabla p_1^{(j)}) + \sigma(p_1^{(j)} - p_2^{(j)}) = f_1, & \text{in } \omega_j, \\ -\operatorname{div}(\kappa_2 \nabla p_2^{(j)}) + \sigma(p_2^{(j)} - p_1^{(j)}) = f_2, & \text{in } \omega_j, \end{cases} \tag{4.1}$$

for $i = 1, 2$. For $\forall \boldsymbol{v} \in \boldsymbol{L}^2_{\widetilde{\kappa}}(\omega_j)$, we define the projection operator $\mathcal{P}^{j,M_j} : \boldsymbol{L}^2_{\widetilde{\kappa}}(\omega_j) \to \boldsymbol{V}^{j,M_j}_{\text{off}}$ by

$$\mathcal{P}^{j,M_j}\boldsymbol{v} = (\mathcal{P}^{j,M_j}v_1, \mathcal{P}^{j,M_j}v_2),\ \mathcal{P}^{j,M_j}v_i = \sum_{k=1}^{M_j} \left(v_i, \psi_{k,i}^{(j)}\right)_j^i \psi_{k,i}^{(j)}. \tag{4.2}$$

The operator $\mathcal{P}^{j,M_j}$ will be a crucial component in the convergence analysis. Given that $\boldsymbol{p}^{(j)} \in \boldsymbol{L}^2_{\widetilde{\kappa}}(\omega_j)$, the function $\boldsymbol{p}^{(j)}$ can be expressed as follows

$$\boldsymbol{p}^{(j)} = (p_1^{(j)}, p_2^{(j)}),\ p_i^{(j)} = \sum_{k=1}^{\infty} \left(p_i^{(j)}, \psi_{k,i}^{(j)}\right)_j^i \psi_{k,i}^{(j)}. \tag{4.3}$$

To derive an error estimate for the dual-continuum solutions, we firstly impose the following assumption on the eigenfunctions.

Assumption 4.1. Assume that $\boldsymbol{f} \in \boldsymbol{L}^2_{\widetilde{\kappa}^{-1}}(\Omega)$ and $g_i \in H^s(\partial\Omega)$ with $s > \frac{3}{2}$. Then there exists a constant $C > 0$ depending on Ω, κ_i, and s, such that:

$$\sum_{k=1}^{\infty} \left(\lambda_k^{(j)}\right)^2 \left(\boldsymbol{p}^{(j)}, \boldsymbol{\psi}_k^{(j)}\right)_j^2 \le \|\boldsymbol{f}\|^2_{\boldsymbol{L}^2_{\widetilde{\kappa}^{-1}}(\omega_j)} + C\,\|\boldsymbol{g}\|^2_{H^s(\partial\Omega)}.$$

where $\|\boldsymbol{g}\|^2_{H^s(\partial\Omega)} := \sum_{i=1}^n \|g_i\|^2_{H^s(\partial\Omega)}$

Similar to [32], we acknowledge that the eigenfunctions $\{(\psi_{k,1}^{(j)}, \kappa_2\psi_{k,2}^{(j)})\}_{j=1}^{\infty}$ forms the orthogonal basis in the weighted space $\boldsymbol{L}^2_{\widetilde{\kappa}}(\omega_j)$. The weighted results are summarized in the following Lemma.

LEMMA 4.2 ([32]). *The series* $\{(\widetilde{\kappa}_1\psi_{k,1}^{(j)}, \widetilde{\kappa}_2\psi_{k,2}^{(j)})\}_{j=1}^{\infty}$ *forms a complete orthogonal basis in* $\boldsymbol{L}^2_{\widetilde{\kappa}^{-1}}(\omega_j)$.

We now give the local approximation property of the operator $\mathcal{P}^{j,M_j}$ in the sense of $L^2_{\widetilde{\kappa}}$ norm and a_Q norm.

PROPOSITION 4.3. *Assume that* $\boldsymbol{f} \in \boldsymbol{L}^2_{\widetilde{\kappa}^{-1}}(\Omega)$. *Let* $\boldsymbol{p}^{(j)}$ *be the solution of equation* (4.1). *Then the projection* $\mathcal{P}^{j,M_j} : \boldsymbol{L}^2_{\widetilde{\kappa}}(\omega_j) \to \boldsymbol{V}^{j,M_j}_{off}$ *defined in* (4.2) *has the following approximation properties*

$$\left\|\boldsymbol{p}^{(j)} - \mathcal{P}^{j,M_j}\boldsymbol{p}^{(j)}\right\|^2_{L^2_{\widetilde{\kappa}}(\omega_j)} \le \left(\lambda_{M_j+1}^{(j)}\right)^{-2} (\|\boldsymbol{f}\|^2_{\boldsymbol{L}^2_{\widetilde{\kappa}^{-1}}(\omega_j)} + C\,\|\boldsymbol{g}\|^2_{H^s(\partial\Omega)}),$$
$$\left\|\boldsymbol{p}^{(j)} - \mathcal{P}^{j,M_j}\boldsymbol{p}^{(j)}\right\|^2_{a_Q(\omega_j)} \le \left(\lambda_{M_j+1}^{(j)}\right)^{-1} (\|\boldsymbol{f}\|^2_{\boldsymbol{L}^2_{\widetilde{\kappa}^{-1}}(\omega_j)} + C\,\|\boldsymbol{g}\|^2_{H^s(\partial\Omega)}).$$

Proof. The definitions (4.2) and (4.3) and the orthonormality of $\{\boldsymbol{\psi}_k^{(j)}\}_{k=1}^{\infty}$ in $\boldsymbol{L}^2_{\widetilde{\kappa}}(\omega_j)$ directly yield

$$\begin{aligned}
\left\|\boldsymbol{p}^{(j)}-\mathcal{P}^{j,M_j}\boldsymbol{p}^{(j)}\right\|^2_{L^2_{\tilde{\kappa}}(\omega_j)} &= \left\|\sum_{k=M_j+1}^{\infty}\left(\left(p_1^{(j)},\psi_{k,1}^{(j)}\right)_j^1\psi_{k,1}^{(j)},\left(p_2^{(j)},\psi_{k,2}^{(j)}\right)_j^2\psi_{k,2}^{(j)}\right)\right\|^2_{L^2_{\tilde{\kappa}}(\omega_j)}\\
&= \sum_{k=M_j+1}^{\infty}\left(\boldsymbol{p}^{(j)},\boldsymbol{\psi}_k^{(j)}\right)_j^2\\
&= \sum_{k=M_j+1}^{\infty}\left(\lambda_k^{(j)}\right)^{-2}\left(\lambda_k^{(j)}\right)^2\left(\boldsymbol{p}^{(j)},\boldsymbol{\psi}_k^{(j)}\right)_j^2\\
&\le \left(\lambda_{M_j+1}^{(j)}\right)^{-2}\sum_{k=M_j+1}^{\infty}\left(\lambda_k^{(j)}\right)^2\left(\boldsymbol{p}^{(j)},\boldsymbol{\psi}_k^{(j)}\right)_j^2\\
&\le \left(\lambda_{M_j+1}^{(j)}\right)^{-2}\left(\|\boldsymbol{f}\|^2_{\boldsymbol{L}^2_{\tilde{\kappa}^{-1}}(\omega_j)}+C\|\boldsymbol{g}\|^2_{H^s(\partial\Omega)}\right),
\end{aligned}$$

where in the last step we have used Assumption 4.1. Similarly, we can obtain

$$\begin{aligned}
\left\|\boldsymbol{p}^{(j)}-\mathcal{P}^{j,M_j}\boldsymbol{p}^{(j)}\right\|^2_{a_Q(\omega_j)} &= \left\|\sum_{k=M_j+1}^{\infty}\left(\left(p_1^{(j)},\psi_{k,1}^{(j)}\right)_j^1\psi_{k,1}^{(j)},\left(p_2^{(j)},\psi_{k,2}^{(j)}\right)_j^2\psi_{k,2}^{(j)}\right)\right\|^2_{a_Q(\omega_j)}\\
&= \sum_{k=M_j+1}^{\infty}\lambda_k^{(j)}\left(\boldsymbol{p}^{(j)},\boldsymbol{\psi}_k^{(j)}\right)_j^2\\
&= \sum_{k=M_j+1}^{\infty}\left(\lambda_k^{(j)}\right)^{-1}\left(\lambda_k^{(j)}\right)^2\left(\boldsymbol{p}^{(j)},\boldsymbol{\psi}_k^{(j)}\right)_j^2\\
&\le \left(\lambda_{M_j+1}^{(j)}\right)^{-1}\sum_{k=M_j+1}^{\infty}\left(\lambda_k^{(j)}\right)^2\left(\boldsymbol{p}^{(j)},\boldsymbol{\psi}_k^{(j)}\right)_j^2\\
&\le \left(\lambda_{M_j+1}^{(j)}\right)^{-1}\left(\|\boldsymbol{f}\|^2_{\boldsymbol{L}^2_{\tilde{\kappa}^{-1}}(\omega_j)}+C\|\boldsymbol{g}\|^2_{H^s(\partial\Omega)}\right).
\end{aligned}$$

This proof is completed. ∎

Subsequently, the global error estimate for the GMsFEM solution will be given in Theorem 4.4.

THEOREM 4.4. *Assume that* $\boldsymbol{f}\in\boldsymbol{L}^2_{\tilde{\kappa}^{-1}}(\Omega)\cap\boldsymbol{L}^2(\Omega)$ *and* M_j *is sufficiently large such that*

$$\lambda_{M_j+1}\ge H^{-2},\ j=1,2,\ldots,N_c.$$

Let $\boldsymbol{p}$ *be the solution of equation* (2.1)*, and* $\boldsymbol{p}^{\mathrm{ms}}$ *be the GMsFEM solution. Then there holds*

$$\|\boldsymbol{p}-\boldsymbol{p}^{\mathrm{ms}}\|^2_{a_Q}\le\tilde{C}_1(H^2+\Lambda^{-1})\|\boldsymbol{f}\|^2_{\boldsymbol{L}^2_{\tilde{\kappa}^{-1}}(\omega_j)}+\tilde{C}_2(H^2+\Lambda^{-1})\|\boldsymbol{g}\|^2_{H^s(\partial\Omega)},$$

where $\Lambda=\min_{1\le j\le N_c}\lambda_{M_j+1}^{(j)}$ *and constants* $\tilde{C}_1$,$\tilde{C}_2$ *is independent of* Λ *and* H.

Proof. Let $\boldsymbol{w}$ be the projection of $\boldsymbol{p}$ in the multiscale finite element space $\boldsymbol{V}_{\mathrm{ms}}$ as follows

$$\boldsymbol{w}(x)=(w_1(x),w_2(x)),\ w_i(x)=\sum_{j=1}^{N_c}\chi_{j,i}(x)\mathcal{P}^{j,M_j}p_i.$$

By Céa's lemma, we have

$$\|\boldsymbol{p}-\boldsymbol{p}^{\mathrm{ms}}\|_{a_Q}^2 \le \|\boldsymbol{p}-\boldsymbol{w}\|_{a_Q}^2.$$

With the property of the partition of unity function $\{\boldsymbol{\chi}_j\}_{j=1}^{N_c}$ and the overlap condition (3.5), we get

$$\begin{aligned}\|\boldsymbol{p}-\boldsymbol{w}\|_{a_Q}^2 &= \left\|\sum_j \boldsymbol{\chi}_j(\boldsymbol{p}-\boldsymbol{w})\right\|_{a_Q}^2 \\ &\le C_{\mathrm{ov}}\sum_{j=1}^{N_c} a_Q^{(j)}\left(\boldsymbol{\chi_j}(\boldsymbol{p}^{(j)}-\mathcal{P}^{j,M_j}\boldsymbol{p}^{(j)}),\boldsymbol{\chi_j}(\boldsymbol{p}^{(j)}-\mathcal{P}^{j,M_j}\boldsymbol{p}^{(j)})\right).\end{aligned}$$

We define $\boldsymbol{e}^{(j)}=\boldsymbol{p}^{(j)}-\mathcal{P}^{j,M_j}\boldsymbol{p}^{(j)}$, where $\boldsymbol{e}^{(j)}=(e_1^{(j)},e_2^{(j)})$ and $e_i^{(j)}=p_i-\mathcal{P}^{j,M_j}p_i$ for $i=1,2$, and arrive at

$$\begin{aligned}&\|\boldsymbol{p}-\boldsymbol{w}\|_{a_Q}^2 \\ &\quad\le C_{\mathrm{ov}}\sum_{j=1}^{N_c} a_Q^{(j)}\left(\boldsymbol{\chi_j}\boldsymbol{e}^{(j)},\boldsymbol{\chi_j}\boldsymbol{e}^{(j)}\right) \\ &\quad\le 2C_{\mathrm{ov}}\sum_{i=1}^{2}\sum_{j=1}^{N_c}\left(\int_{\omega_j}\kappa_i\left|\nabla\chi_{j,i}\right|^2\left|e_i^{(j)}\right|^2\,\mathrm{d}x+\int_{\omega_j}\kappa_i\left|\chi_{j,i}\right|^2\left|\nabla e_i^{(j)}\right|^2\,\mathrm{d}x\right) \\ &\qquad+2C_{\mathrm{ov}}\sum_{i=1}^{2}\sum_{l=1}^{2}\sum_{j=1}^{N_c}\int_{\omega_j}\sigma\left(\chi_{j,i}e_i^{(j)}-\chi_{j,l}e_l^{(j)}\right)\left(\chi_{j,i}e_i^{(j)}\right)\,\mathrm{d}x \\ &\quad= 2C_{\mathrm{ov}}\sum_{i=1}^{2}\sum_{j=1}^{N_c}\left(H^{-2}\int_{\omega_j}H^2\kappa_i\left|\nabla\chi_{j,i}\right|^2\left|e_i^{(j)}\right|^2\,\mathrm{d}x+\int_{\omega_j}\kappa_i\left|\chi_{j,i}\right|^2\left|\nabla e_i^{(j)}\right|^2\,\mathrm{d}x\right) \\ &\qquad+2C_{\mathrm{ov}}\sum_{i=1}^{2}\sum_{l=1}^{2}\sum_{j=1}^{N_c}\int_{\omega_j}\sigma\left(\chi_{j,i}e_i^{(j)}-\chi_{j,l}e_l^{(j)}\right)\left(\chi_{j,i}e_i^{(j)}\right)\,\mathrm{d}x.\end{aligned}$$

By Proposition 4.3, the overlap condition (3.5), and assumption, we have

$$\begin{aligned}&\|\boldsymbol{p}-\boldsymbol{p}_{\mathrm{ms}}\|_{a_Q}^2 \\ &\quad\le 2C_{\mathrm{ov}}\sum_{j=1}^{N_c}\left(H^{-2}\left(\lambda_{M_j+1}^{(j)}\right)^{-2}+\left(\lambda_{M_j+1}^{(j)}\right)^{-1}\right)\left(\|\boldsymbol{f}\|_{\boldsymbol{L}^2_{\tilde{\kappa}^{-1}}(\omega_j)}^2+C\|\boldsymbol{g}\|_{H^s(\partial\Omega)}^2\right) \\ &\quad\le 2C_{\mathrm{ov}}^2\max_{1\le j\le N_c}\left\{H^{-2}\left(\lambda_{M_j+1}^{(j)}\right)^{-2}+\left(\lambda_{M_j+1}^{(j)}\right)^{-1}\right\}\left(\|\boldsymbol{f}\|_{\boldsymbol{L}^2_{\tilde{\kappa}^{-1}}(\omega_j)}^2+C\|\boldsymbol{g}\|_{H^s(\partial\Omega)}^2\right) \\ &\quad\le 2C_{\mathrm{ov}}^2\max_{1\le j\le N_c}\left\{H^2+\left(\lambda_{M_j+1}^{(j)}\right)^{-1}\right\}\left(\|\boldsymbol{f}\|_{\boldsymbol{L}^2_{\tilde{\kappa}^{-1}}(\omega_j)}^2+C\|\boldsymbol{g}\|_{H^s(\partial\Omega)}^2\right) \\ &\quad\le \tilde{C}_1(H^2+\Lambda^{-1})\|\boldsymbol{f}\|_{\boldsymbol{L}^2_{\tilde{\kappa}^{-1}}(\omega_j)}^2+\tilde{C}_2(H^2+\Lambda^{-1})\|\boldsymbol{g}\|_{H^s(\partial\Omega)}^2 \\ &\quad\le \tilde{C}_1(H^2+\Lambda^{-1})\|\boldsymbol{f}\|_{\boldsymbol{L}^2_{\tilde{\kappa}^{-1}}(\Omega)}^2+\tilde{C}_2(H^2+\Lambda^{-1})\|\boldsymbol{g}\|_{H^s(\partial\Omega)}^2.\end{aligned}$$

Here, $\Lambda=\min_{1\le j\le N_c}\lambda_{M_j+1}^{(j)}$ and constants $\tilde{C}_1$,$\tilde{C}_2$ is independent of Λ and H.

This proof is completed. ∎

Next, we will study an error estimate for the dual-continuum model with random input. Firstly, the following norm equivalence between $\|\nabla \boldsymbol{p}\|_{\boldsymbol{L}^2(\Omega)}$ and $\|\boldsymbol{p}\|_{a_Q}$ is demonstrated, where diffusion coefficients of the $\|\cdot\|_{a_Q}$ is κ_i^0 for $i=1,2$.

LEMMA 4.5. *Assume that* $\underline{\kappa^0} - 2\overline{\sigma} C_p^2 > 0$, *there exist constants* $\alpha_0 > 0$ *and* $\beta_0 > 0$, *for each* $\boldsymbol{v} \in \boldsymbol{V}$ *such that*

$$\alpha_0 \|\nabla \boldsymbol{v}\|_{\boldsymbol{L}^2(\Omega)} \le \|\boldsymbol{v}\|_{a_Q} \le \beta_0 \|\nabla \boldsymbol{v}\|_{\boldsymbol{L}^2(\Omega)}.$$

Here, $\alpha_0 = (\underline{\kappa^0} - 2\overline{\sigma} C_p^2)^{\frac{1}{2}}$, $\beta_0 = (\overline{\kappa^0} + 2\overline{\sigma} C_p^2)^{\frac{1}{2}}$ *and* $\overline{\kappa^0} = \max_{x\in\Omega, \boldsymbol{\xi}\in D, i=1,2} \kappa_i(x, \boldsymbol{\xi})$.

The proof of Lemma 4.5 is described in Appendix A. In [36], there holds the following Lax Milgram theorem under Assumption 2.1.

THEOREM 4.6. *Under Assumption* 2.1, *the problem* (2.2) *has a unique solution* $\boldsymbol{p}(\boldsymbol{\xi}) \in \boldsymbol{V}$ *for each* $\boldsymbol{\xi} \in D$ *with respect to the norm* $\|\cdot\|_{a_Q}$, *and there holds*

$$\|\boldsymbol{p}(\boldsymbol{\xi})\|_{a_Q} \le \tilde{C}_3 \|\boldsymbol{f}\|_{\boldsymbol{L}^2(\Omega)}, \ \forall \boldsymbol{\xi} \in D,$$

where the constant $\tilde{C}_3$ *is independent of the parameter* $\boldsymbol{\xi}$.

Based on the preceding Lemma 4.5 and Theorem 4.6, we can derive the convergence of the sequence $\{\boldsymbol{P}_n(\boldsymbol{\xi})\}_{n\ge 0}$ generated by the iterative method as stated in the following theorem.

THEOREM 4.7. *Assume that there is a constant* $\rho \in (0,1)$ *s.t.* $\rho \ge \frac{\overline{\kappa^1}}{\underline{\kappa^0} - 2\overline{\sigma} C_p^2}$, *let* $\boldsymbol{p}(\boldsymbol{\xi})$ *be the solution of* (2.2) *and* $\{\boldsymbol{P}_n(\boldsymbol{\xi})\}_{n\ge 0}$ *be generated by the iterative method. There exists a constant* $\tilde{C}_3 \ge 0$ *such that*

$$\|\boldsymbol{p}(\boldsymbol{\xi}) - \boldsymbol{P}_n(\boldsymbol{\xi})\|_{a_Q} \le \tilde{C}_3 \rho^{n+1} \|\boldsymbol{f}\|_{\boldsymbol{L}^2(\Omega)}, \ \forall \boldsymbol{\xi} \in D.$$

Proof. For each fixed $\boldsymbol{\xi} \in D$, let $\boldsymbol{r}_n = \boldsymbol{r}_n(\boldsymbol{\xi}) = \boldsymbol{p}(\boldsymbol{\xi}) - \boldsymbol{P}_n(\boldsymbol{\xi}) \in \boldsymbol{V}$ for $n \ge 0$. Then, subtracting (3.1) from (3.2) yields the following error equation for $n = 0$

$$a^0(\boldsymbol{r}_0, \boldsymbol{v}) + q(\boldsymbol{r}_0, \boldsymbol{v}) = -a^1(\boldsymbol{p}, \boldsymbol{v}; \boldsymbol{\xi}), \ \forall \boldsymbol{v} \in \boldsymbol{V}. \tag{4.4}$$

Similarly, subtracting (3.1) from (3.3) yields the following error equation for $n > 0$

$$a^0(\boldsymbol{r}_n, \boldsymbol{v}) + q(\boldsymbol{r}_n, \boldsymbol{v}) = -a^1(\boldsymbol{r}_{n-1}, \boldsymbol{v}; \boldsymbol{\xi}), \ \forall \boldsymbol{v} \in \boldsymbol{V}. \tag{4.5}$$

Choosing $\boldsymbol{v} = \boldsymbol{r}_0$ in (4.4), we obtain

$$a^0(\boldsymbol{r}_0, \boldsymbol{r}_0) + q(\boldsymbol{r}_0, \boldsymbol{r}_0) = -a^1(\boldsymbol{p}, \boldsymbol{r}_0; \boldsymbol{\xi}).$$

That is

$$\|\boldsymbol{r}_0\|_{a_Q}^2 = -a^1(\boldsymbol{p}, \boldsymbol{r}_0; \boldsymbol{\xi}). \tag{4.6}$$

By the Cauchy–Schwarz inequality and Lemma 4.5, we derive the inequality

$$\begin{aligned} |-a^1(\boldsymbol{p}, \boldsymbol{r}_0; \boldsymbol{\xi})| &\le \overline{\kappa^1} \|\nabla \boldsymbol{p}\|_{\boldsymbol{L}^2(\Omega)} \|\nabla \boldsymbol{r}_0\|_{\boldsymbol{L}^2(\Omega)} \\ &\le \frac{\overline{\kappa^1}}{(\alpha_0)^2} \|\boldsymbol{p}\|_{a_Q} \|\boldsymbol{r}_0\|_{a_Q}. \end{aligned}$$

Combining the above inequality with (4.6), we can obtain

$$\|\boldsymbol{r}_0\|_{a_Q} \le \frac{\overline{\kappa^1}}{(\alpha_0)^2} \|\boldsymbol{p}\|_{a_Q} \le \rho \|\boldsymbol{p}\|_{a_Q}.$$

We also choose $\boldsymbol{v} = \boldsymbol{r}_n$ in (4.4) and obtain

$$a^0(\boldsymbol{r}_n, \boldsymbol{r}_n) + q(\boldsymbol{r}_n, \boldsymbol{r}_n) = -a^1(\boldsymbol{r}_{n-1}, \boldsymbol{r}_n; \boldsymbol{\xi}). \tag{4.7}$$

Similarly, by (4.7), we can obtain

$$\|\boldsymbol{r}_n\|_{a_Q} \leq \frac{\overline{\kappa^1}}{(\alpha_0)^2}\|\boldsymbol{r}_{n-1}\|_{a_Q} \leq \rho\|\boldsymbol{r}_{n-1}\|_{a_Q}.$$

By induction and Theorem 4.6, we have

$$\|\boldsymbol{r}_n\|_{a_Q} \leq \rho^{n+1}\|\boldsymbol{p}\|_{a_Q} \leq \tilde{C}_3\rho^{n+1}\|\boldsymbol{f}\|_{\boldsymbol{L}^2(\Omega)}.$$

This completes the proof. ∎

To establish the error estimates for the Iter-GMsFE solutions $\{\boldsymbol{P}_n^{\mathrm{ms}}(\boldsymbol{\xi})\}_{n\geq 0}$, we provide the following lemma.

LEMMA 4.8. *Under the assumption of Theorem* 4.7*, let* $\{\boldsymbol{P}_n(\boldsymbol{\xi})\}_{n\geq 0}$ *be generated by the iterative method. We have*

$$\|\boldsymbol{P}_n(\boldsymbol{\xi})\|_{a_Q} \leq \tilde{C}_4\|\boldsymbol{f}\|_{\boldsymbol{L}^2(\Omega)},$$

where the constant $\tilde{C}_4$ *is independent of* $\boldsymbol{\xi}$*.*

Proof. By Theorem 4.6, the following estimation can be given

$$\|\boldsymbol{P}_0(\boldsymbol{\xi})\|_{a_Q} \leq \tilde{C}_3\|\boldsymbol{f}\|_{\boldsymbol{L}^2(\Omega)}.$$

Choosing $\boldsymbol{v} = \boldsymbol{P}_n$ in (3.3), and based on Cauchy–Schwarz inequality, we obtain

$$\begin{aligned}
\|\boldsymbol{P}_n\|_{a_Q}^2 &= a^0(\boldsymbol{P}_n, \boldsymbol{P}_n) + q(\boldsymbol{P}_n, \boldsymbol{P}_n) \\
&= b(\boldsymbol{P}_n) - a^1(\boldsymbol{P}_{n-1}, \boldsymbol{P}_n) \\
&\leq \|\boldsymbol{P}_n\|_{\boldsymbol{L}^2(\Omega)}\|\boldsymbol{f}\|_{\boldsymbol{L}^2(\Omega)} + \overline{\kappa^1}\|\nabla\boldsymbol{P}_{n-1}\|_{\boldsymbol{L}^2(\Omega)}\|\nabla\boldsymbol{P}_n\|_{\boldsymbol{L}^2(\Omega)} \\
&\leq \frac{1}{\alpha_0}\|\boldsymbol{P}_n\|_{a_Q}\|\boldsymbol{f}\|_{\boldsymbol{L}^2(\Omega)} + \frac{\overline{\kappa^1}}{(\alpha_0)^2}\|\boldsymbol{P}_n\|_{a_Q}\|\boldsymbol{P}_{n-1}\|_{a_Q}.
\end{aligned}$$

Then, dividing both sides of above inequality by $\|\boldsymbol{P}_n\|_{a_Q}$, we have

$$\|\boldsymbol{P}_n\|_{a_Q} \leq \frac{1}{\alpha_0}\|\boldsymbol{f}\|_{\boldsymbol{L}^2(\Omega)} + \frac{\overline{\kappa^1}}{(\alpha_0)^2}\|\boldsymbol{P}_{n-1}\|_{a_Q}.$$

By induction, we have

$$\begin{aligned}
\|\boldsymbol{P}_n\|_{a_Q} &\leq \frac{1}{\alpha_0}\left(\sum_{i=1}^{n-1}\left(\frac{\overline{\kappa^1}}{\alpha_0^2}\right)^i + 1\right)\|\boldsymbol{f}\|_{\boldsymbol{L}^2(\Omega)} + \left(\frac{\overline{\kappa^1}}{\alpha_0^2}\right)^n\|\boldsymbol{P}_0\|_{a_Q} \\
&\leq \frac{1}{\alpha_0}\left(\sum_{i=1}^{n-1}\left(\frac{\overline{\kappa^1}}{\alpha_0^2}\right)^i + 1\right)\|\boldsymbol{f}\|_{\boldsymbol{L}^2(\Omega)} + \tilde{C}_3\left(\frac{\overline{\kappa^1}}{\alpha_0^2}\right)^n\|\boldsymbol{f}\|_{\boldsymbol{L}^2(\Omega)} \\
&\leq \tilde{C}_4\|\boldsymbol{f}\|_{\boldsymbol{L}^2(\Omega)},
\end{aligned}$$

where $\tilde{C}_4 = \tilde{C}_3\rho^n + \frac{1-\rho^n}{\alpha_0(1-\rho)}$, which implies that $\tilde{C}_4$ is bounded due to $\rho < 1$. Then the convergence of the iterative method can be guaranteed.

This proof is completed. ∎

THEOREM 4.9. *Under the assumptions of Theorem* 4.4 *and Theorem* 4.7*, let* $\{\boldsymbol{P}_n(\boldsymbol{\xi})\}_{n\geq 0}$ *be generated by the iterative method and* $\{\boldsymbol{P}_n^{\mathrm{ms}}(\boldsymbol{\xi})\}_{n\geq 0}$ *be generated by Iter-GMsFEM. Then there holds*

$$\|\boldsymbol{P}_n(\boldsymbol{\xi})-\boldsymbol{P}_n^{\mathrm{ms}}(\boldsymbol{\xi})\|_{a_Q}^2 \leq \tilde{C}_5(H^2+\Lambda^{-1})\|\boldsymbol{f}\|_{\boldsymbol{L}^2(\Omega)}^2+\tilde{C}_6\|\boldsymbol{g}\|_{H^s(\partial\Omega)}^2,$$

where the constants $\tilde{C}_5$ *and* $\tilde{C}_6$ *are independent of the size of the mesh girds* H *and* h*, the iterative number* n *and parameter* $\boldsymbol{\xi}$*, and* $\Lambda=\min_{1\leq j\leq N_c}\{\lambda_{M_j+1}^{(j)}\}$.

Proof. For $n=0$ and each parameter $\boldsymbol{\xi}$, due to a_0 being parameter-independent and Theorem 4.4, we have

$$\|\boldsymbol{P}_0-\boldsymbol{P}_0^{\mathrm{ms}}\|_{a_Q}^2 \leq \tilde{C}_1(H^2+\Lambda^{-1})\|\boldsymbol{f}\|_{\boldsymbol{L}^2_{\tilde{\kappa}^{-1}}(\Omega)}^2+\tilde{C}_2(H^2+\Lambda^{-1})\|\boldsymbol{g}\|_{H^s(\partial\Omega)}^2. \tag{4.8}$$

For $n\geq 1$ and each parameter $\boldsymbol{\xi}$, we define the auxiliary function $\hat{\boldsymbol{P}}_n^{\mathrm{ms}}=\hat{\boldsymbol{P}}_n^{\mathrm{ms}}(\boldsymbol{\xi})\in\boldsymbol{V}_{\mathrm{ms}}$ as the solution of the following variational form,

$$a^0(\hat{\boldsymbol{P}}_n^{\mathrm{ms}}(\boldsymbol{\xi}),\boldsymbol{v})+q(\hat{\boldsymbol{P}}_n^{\mathrm{ms}}(\boldsymbol{\xi}),\boldsymbol{v})=b(\boldsymbol{v};\boldsymbol{\xi})-a^1(\boldsymbol{P}_{n-1}(\boldsymbol{\xi}),\boldsymbol{v};\boldsymbol{\xi}),\ \forall\boldsymbol{v}\in\boldsymbol{V}_{\mathrm{ms}}. \tag{4.9}$$

Then, for each fixed parameter $\boldsymbol{\xi}$, we have

$$\boldsymbol{P}_n-\boldsymbol{P}_n^{\mathrm{ms}}=\boldsymbol{P}_n-\hat{\boldsymbol{P}}_n^{\mathrm{ms}}+\hat{\boldsymbol{P}}_n^{\mathrm{ms}}-\boldsymbol{P}_n^{\mathrm{ms}}.$$

By Theorem 4.4, we have

$$\begin{aligned}
&\|\boldsymbol{P}_n-\hat{\boldsymbol{P}}_n^{\mathrm{ms}}\|_{a_Q}^2\\
&\quad\leq\tilde{C}_1(H^2+\Lambda^{-1})\left(\|\boldsymbol{f}\|_{\boldsymbol{L}^2_{\tilde{\kappa}_0^{-1}}(\Omega)}^2+\sum_{i=1}^{2}\|(\kappa_i^1)^{\frac{1}{2}}(\kappa_i^0)^{-\frac{1}{2}}\nabla P_{n,i}\|_{L^2(\Omega)}\right)\\
&\qquad+\tilde{C}_2(H^2+\Lambda^{-1})\|\boldsymbol{g}\|_{H^s(\partial\Omega)}^2\\
&\quad\leq\tilde{C}_1(H^2+\Lambda^{-1})\left(\|\boldsymbol{f}\|_{\boldsymbol{L}^2_{\tilde{\kappa}_0^{-1}}(\Omega)}^2+\frac{\sqrt{\overline{\kappa^1}}}{\sqrt{\underline{\kappa^0}}}\|\nabla\boldsymbol{P}_n\|_{\boldsymbol{L}^2(\Omega)}\right)+\tilde{C}_2(H^2+\Lambda^{-1})\|\boldsymbol{g}\|_{H^s(\partial\Omega)}^2\\
&\quad\leq\tilde{C}_1(H^2+\Lambda^{-1})\left(\frac{1}{\sqrt{\underline{\kappa^0}}}\|\boldsymbol{f}\|_{\boldsymbol{L}^2(\Omega)}^2+\frac{\sqrt{\overline{\kappa^1}}}{\alpha_0\sqrt{\underline{\kappa^0}}}\|\boldsymbol{P}_n\|_{a_Q}\right)+\tilde{C}_2(H^2+\Lambda^{-1})\|\boldsymbol{g}\|_{H^s(\partial\Omega)}^2.
\end{aligned}$$

By Lemma 4.8, we deduce

$$\begin{aligned}
\|\boldsymbol{P}_n-\hat{\boldsymbol{P}}_n^{\mathrm{ms}}\|_{a_Q}^2 \leq{}& \tilde{C}_1(H^2+\Lambda^{-1})(\underline{\kappa^0})^{-\frac{1}{2}}\left(1+\rho^{\frac{1}{2}}\tilde{C}_4\right)\|\boldsymbol{f}\|_{\boldsymbol{L}^2(\Omega)}\\
&+\tilde{C}_2(H^2+\Lambda^{-1})\|\boldsymbol{g}\|_{H^s(\partial\Omega)}^2.
\end{aligned} \tag{4.10}$$

Subsequently, we give the error estimate between $\hat{\boldsymbol{P}}_n^{\mathrm{ms}}$ and $\boldsymbol{P}_n^{\mathrm{ms}}$. For each given parameter $\boldsymbol{\xi}$, combining (3.12) with (4.9), it follows that

$$\begin{aligned}
&a^0(\hat{\boldsymbol{P}}_n^{\mathrm{ms}}(\boldsymbol{\xi})-\boldsymbol{P}_n^{\mathrm{ms}}(\boldsymbol{\xi}),\boldsymbol{v})+q(\hat{\boldsymbol{P}}_n^{\mathrm{ms}}(\boldsymbol{\xi})-\boldsymbol{P}_n^{\mathrm{ms}}(\boldsymbol{\xi}),\boldsymbol{v})\\
&\quad=-a^1(\boldsymbol{P}_{n-1}(\boldsymbol{\xi})-\boldsymbol{P}_{n-1}^{\mathrm{ms}}(\boldsymbol{\xi}),\boldsymbol{v};\boldsymbol{\xi}),\ \forall\boldsymbol{v}\in\boldsymbol{V}_{\mathrm{ms}}.
\end{aligned}$$

Let $\boldsymbol{v}=\hat{\boldsymbol{P}}_n^{\mathrm{ms}}(\boldsymbol{\xi})-\boldsymbol{P}_n^{\mathrm{ms}}(\boldsymbol{\xi})\in\boldsymbol{V}_{\mathrm{ms}}$, by definition of a_Q norm and Cauchy–Schwarz inequality, we obtain

$$\|\hat{\boldsymbol{P}}_n^{\mathrm{ms}}(\boldsymbol{\xi})-\boldsymbol{P}_n^{\mathrm{ms}}(\boldsymbol{\xi})\|_{a_Q}^2\leq\overline{\kappa^1}\|\boldsymbol{P}_{n-1}(\boldsymbol{\xi})-\boldsymbol{P}_{n-1}^{\mathrm{ms}}(\boldsymbol{\xi})\|_{\boldsymbol{L}^2(\Omega)}\|\hat{\boldsymbol{P}}_n^{\mathrm{ms}}(\boldsymbol{\xi})-\boldsymbol{P}_n^{\mathrm{ms}}(\boldsymbol{\xi})\|_{\boldsymbol{L}^2(\Omega)}.$$

Then, dividing both sides of above in inequality by $\|\hat{\boldsymbol{P}}_n^{\mathrm{ms}}(\boldsymbol{\xi}) - \boldsymbol{P}_n^{\mathrm{ms}}(\boldsymbol{\xi})\|_{a_Q}^2$, we have

$$\|\hat{\boldsymbol{P}}_n^{\mathrm{ms}}(\boldsymbol{\xi}) - \boldsymbol{P}_n^{\mathrm{ms}}(\boldsymbol{\xi})\|_{a_Q} \leq \frac{\overline{\kappa^1}}{(\alpha_0)^2}\|\boldsymbol{P}_{n-1}(\boldsymbol{\xi}) - \boldsymbol{P}_{n-1}^{\mathrm{ms}}(\boldsymbol{\xi})\|_{a_Q}. \tag{4.11}$$

Combining (4.10) with (4.11), we get

$$\begin{aligned}
&\|\boldsymbol{P}_n(\boldsymbol{\xi}) - \boldsymbol{P}_n^{\mathrm{ms}}(\boldsymbol{\xi})\|_{a_Q}^2 \\
&\quad\leq \|\boldsymbol{P}_n(\boldsymbol{\xi}) - \hat{\boldsymbol{P}}_n^{\mathrm{ms}}(\boldsymbol{\xi})\|_{a_Q}^2 + \|\hat{\boldsymbol{P}}_n^{\mathrm{ms}}(\boldsymbol{\xi} - \boldsymbol{P}_n^{\mathrm{ms}}(\boldsymbol{\xi})\|_{a_Q}^2 \\
&\quad\leq \tilde{C}_1(H^2+\Lambda^{-1})(\underline{\kappa}^0)^{-\frac{1}{2}}\left(1+\rho^{\frac{1}{2}}\tilde{C}_4\right)\|\boldsymbol{f}\|_{\boldsymbol{L}^2(\Omega)}^2 + \tilde{C}_2(H^2+\Lambda^{-1})\|\boldsymbol{g}\|_{H^s(\partial\Omega)}^2 \\
&\qquad+ \frac{\overline{\kappa^1}}{(\alpha_0)^2}\|\boldsymbol{P}_{n-1}(\boldsymbol{\xi}) - \boldsymbol{P}_{n-1}^{\mathrm{ms}}(\boldsymbol{\xi})\|_{a_Q}^2.
\end{aligned}$$

By induction, we have

$$\begin{aligned}
&\|\boldsymbol{P}_n(\boldsymbol{\xi}) - \boldsymbol{P}_n^{\mathrm{ms}}(\boldsymbol{\xi})\|_{a_Q} \\
&\quad\leq (H^2+\Lambda^{-1})\left(1+\sum_{i=1}^{n-1}\rho^i\right)\left(\tilde{C}_1(\underline{\kappa}^0)^{-\frac{1}{2}}(1+\rho^{\frac{1}{2}}\tilde{C}_4)\|\boldsymbol{f}\|_{\boldsymbol{L}^2(\Omega)}^2 + \tilde{C}_2\|\boldsymbol{g}\|_{H^s(\partial\Omega)}^2\right) \\
&\qquad+ \rho^n\|\boldsymbol{P}_0(\boldsymbol{\xi}) - \boldsymbol{P}_0^{\mathrm{ms}}(\boldsymbol{\xi})\|_{a_Q}^2.
\end{aligned}$$

The last inequality is due to the induction. By (4.8), we have

$$\begin{aligned}
&\|\boldsymbol{P}_n(\boldsymbol{\xi}) - \boldsymbol{P}_n^{\mathrm{ms}}(\boldsymbol{\xi})\|_{a_Q}^2 \\
&\quad\leq (H^2+\Lambda^{-1})\left(1+\sum_{i=1}^{n-1}\rho^i\right)\left(\tilde{C}_1(\underline{\kappa}^0)^{-\frac{1}{2}}(1+\rho^{\frac{1}{2}}\tilde{C}_4)\|\boldsymbol{f}\|_{\boldsymbol{L}^2(\Omega)}^2 + \tilde{C}_2\|\boldsymbol{g}\|_{H^s(\partial\Omega)}^2\right) \\
&\qquad+ \rho^n(H^2+\Lambda^{-1})\left(\tilde{C}_1(\underline{\kappa}^0)^{-\frac{1}{2}}(1+\rho^{\frac{1}{2}}\tilde{C}_4)\|\boldsymbol{f}\|_{\boldsymbol{L}^2(\Omega)}^2 + \tilde{C}_2\|\boldsymbol{g}\|_{H^s(\partial\Omega)}^2\right) \\
&\quad\leq (H^2+\Lambda^{-1})\left(\frac{1-\rho^n}{1-\rho}+\rho^n\right)\left(\tilde{C}_1(\underline{\kappa}^0)^{-\frac{1}{2}}(1+\rho^{\frac{1}{2}}\tilde{C}_4)\|\boldsymbol{f}\|_{\boldsymbol{L}^2(\Omega)}^2 + \tilde{C}_2\|\boldsymbol{g}\|_{H^s(\partial\Omega)}^2\right), \\
&\quad\leq \tilde{C}_5(H^2+\Lambda^{-1})\|\boldsymbol{f}\|_{\boldsymbol{L}^2(\Omega)}^2 + \tilde{C}_6\|\boldsymbol{g}\|_{H^s(\partial\Omega)}^2.
\end{aligned}$$

where $\tilde{C}_5 = (\frac{1-\rho^n}{1-\rho}+\rho^n)(\tilde{C}_1(\underline{\kappa}^0)^{-\frac{1}{2}}(1+\rho^{\frac{1}{2}}\tilde{C}_4))$, $\tilde{C}_6 = \tilde{C}_2(\frac{1-\rho^n}{1-\rho}+\rho^n)$, which implies that both $\tilde{C}_5$ and $\tilde{C}_6$ is bounded due to $\rho < 1$.

This proof is completed. ∎

An immediate corollary is obtained as follows.

THEOREM 4.10. *Under the assumptions of Theorem* 4.4 *and Theorem* 4.7, *let* $\boldsymbol{p}(\boldsymbol{\xi})$ *be solution of* (2.2) *and* $\{\boldsymbol{P}_n^{\mathrm{ms}}(\boldsymbol{\xi})\}_{n\geq 0}$ *be generated by Algorithm* 3.3. *Then, there holds*

$$\|\boldsymbol{p}(\boldsymbol{\xi}) - \boldsymbol{P}_n^{\mathrm{ms}}(\boldsymbol{\xi})\|_{a_Q}^2 \leq \tilde{C}_7(\rho^n + H^2 + \Lambda^{-1})\left(\|\boldsymbol{f}\|_{\boldsymbol{L}^2(\Omega)}^2 + \tilde{C}_6\|\boldsymbol{g}\|_{H^s(\partial\Omega)}^2\right),\ \forall \boldsymbol{\xi} \in D,$$

where the constant $\tilde{C}_7$ *is independent of* ρ, Λ, $\boldsymbol{\xi}$, *and* n.

Proof. The proof follows from Theorem 4.7, Theorem 4.9, and an application of the triangle inequality to the decomposition $\boldsymbol{p}(\boldsymbol{\xi}) - \boldsymbol{P}_n^{\mathrm{ms}}(\boldsymbol{\xi}) = (\boldsymbol{p}(\boldsymbol{\xi}) - \boldsymbol{P}_n(\boldsymbol{\xi})) + (\boldsymbol{P}_n(\boldsymbol{\xi}) - \boldsymbol{P}_n^{\mathrm{ms}}(\boldsymbol{\xi}))$. ∎

5. Numerical examples. In this section, we present two numerical examples to demonstrate the applicability of the proposed iterative method for parameter-dependent dual continuum model and to validate the theoretical results. In subsection 5.1, we study the effects of coarse mesh size and number of local basis function on the quality of the approximations. By changing the conductivity values in the background of diffusion coefficient, the convergence condition of the proposed iterative method are numerically verified. In subsection 5.2, we compute the dual-continuum model with the Iter-GMsFEM. In this case, all the diffusion coefficients and source terms are random fields with high dimensional parameters. To demonstrate the theoretical convergence result of our presented iterative method, we will list the relative errors and convergence rate in this example.

5.1. Experiment 1. The computational domain is a 2-D unit square $\Omega = [0,1]^2$. We consider the parameter-dependent dual-continuum model under steady state as

(5.1)
$$\begin{cases} -\operatorname{div}(\kappa_1(x,\boldsymbol{\xi})\nabla p_1(x,\boldsymbol{\xi})) + \sigma(x)\,(p_1(x,\boldsymbol{\xi}) - p_2(x,\boldsymbol{\xi})) = f_1(x,\boldsymbol{\xi}),\ x\in\Omega, \\ \qquad\qquad p_1(x,\boldsymbol{\xi})|_{\partial\Omega} = (1+2\boldsymbol{\xi})(x_1^2+x_2^2), \\ -\operatorname{div}(\kappa_2(x,\boldsymbol{\xi})\nabla p_2(x,\boldsymbol{\xi})) - \sigma(x)\,(p_1(x,\boldsymbol{\xi}) - p_2(x,\boldsymbol{\xi})) = f_2(x,\boldsymbol{\xi}),\ x\in\Omega, \\ \qquad\qquad p_2(x,\boldsymbol{\xi})|_{\partial\Omega} = (1+\boldsymbol{\xi})((x_1-1)^2+(x_2-1)^2), \end{cases}$$

where the diffusion coefficients $\kappa_i(x;\boldsymbol{\xi})$ $(i=1,2)$ and transfer function $\sigma(x)$ are

$$\begin{cases} \kappa_1(x,\boldsymbol{\xi}) = \kappa_1^0(x) + (1+\boldsymbol{\xi}^3)(2+x_1^2+x_2), \\ \kappa_2(x,\boldsymbol{\xi}) = \kappa_2^0(x) + (1+\boldsymbol{\xi}^2)(1+x_1)(1+x_2^2), \\ \sigma(x) = 1 + x_1^2x_2^2, \end{cases}$$

and source terms are given as

$$\begin{cases} f_1(x,\boldsymbol{\xi}) = (2\boldsymbol{\xi}+\boldsymbol{\xi}^2)(1+x_1+x_2) + (\boldsymbol{\xi}+3\boldsymbol{\xi}^2)x_1^2x_2^2(1-x_1-x_2), \\ f_2(x,\boldsymbol{\xi}) = (2+\boldsymbol{\xi}^2)(x_1+x_2-1) + (1+2\boldsymbol{\xi})x_1^2x_2^2(x_1+x_2-1), \end{cases}$$

respectively.

Here $x=(x_1,x_2)\in\Omega$ and the random variable $\boldsymbol{\xi}$ obeys the uniform distribution, i.e., $\boldsymbol{\xi}\sim U(0,1)$. The diffusion coefficients $\kappa_1^0(x)$ and $\kappa_2^0(x)$ are both high-contrast functions independent of $\boldsymbol{\xi}$ with contrastness $\eta = 10^5$, whose maps are depicted in Figure 2. The conductivity values in the background are both fixed to be 20, where the conductivity values in the channels are high.

In this example, we use 120×120 uniform fine grid to compute the reference solutions $\boldsymbol{p}^{\mathrm{ref}}(x,\boldsymbol{\xi}_j) = (p_1^{\mathrm{ref}}(x,\boldsymbol{\xi}_j), p_2^{\mathrm{ref}}(x,\boldsymbol{\xi}_j))$. The number of degrees freedom $N_f = 14641$. The GMsFEM solutions $\boldsymbol{p}^{\mathrm{gms}}(x,\boldsymbol{\xi}_j) = (p_1^{\mathrm{gms}}(x,\boldsymbol{\xi}_j), p_2^{\mathrm{gms}}(x,\boldsymbol{\xi}_j))$ are computed on 12×12 coarse mesh, and $\boldsymbol{p}^{\mathrm{Iter-GMs}}(x,\boldsymbol{\xi}_j) = (p_1^{\mathrm{Iter-GMs}}(x,\boldsymbol{\xi}_j), p_2^{\mathrm{Iter-GMs}}(x,\boldsymbol{\xi}_j))$ are solutions by the proposed iterative method. To measure the errors between the reference solutions and numerical solutions, we define the relative L^2-errors as

(5.2)
$$\begin{cases} e_p^{i,\mathrm{gms}} = \dfrac{1}{N}\displaystyle\sum_{j=1}^{N} \frac{\|p_i^{\mathrm{ref}}(x,\boldsymbol{\xi}_j) - p_i^{\mathrm{gms}}(x,\boldsymbol{\xi}_j\|_{L^2(\Omega)}}{\|p_i^{\mathrm{ref}}(x,\boldsymbol{\xi}_j)\|_{L^2(\Omega)}}, \\ e_p^{i,\mathrm{Iter-GMs}} = \dfrac{1}{N}\displaystyle\sum_{j=1}^{N} \frac{\|p_i^{\mathrm{ref}}(x,\boldsymbol{\xi}_j) - p_i^{\mathrm{Iter-GMs}}(x,\boldsymbol{\xi}_j\|_{L^2(\Omega)}}{\|p_i^{\mathrm{ref}}(x,\boldsymbol{\xi}_j)\|_{L^2(\Omega)}}, \end{cases}$$

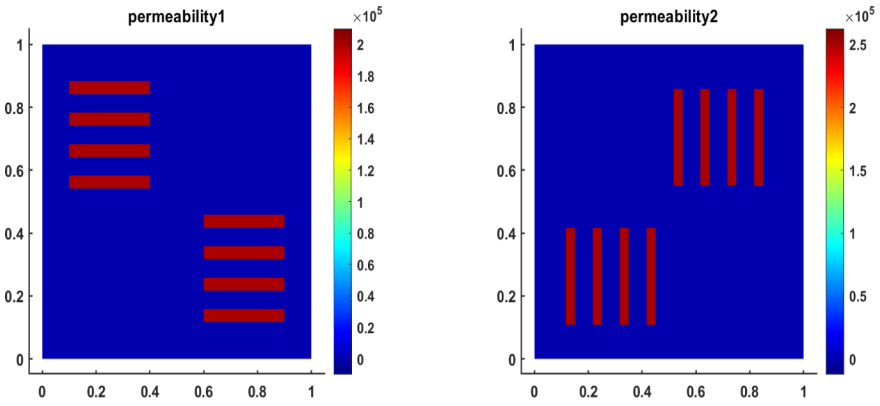

FIG. 2. *High-contrast functions* $\kappa_1^0(x)$ *(left) and* $\kappa_2^0(x)$ *(right).*

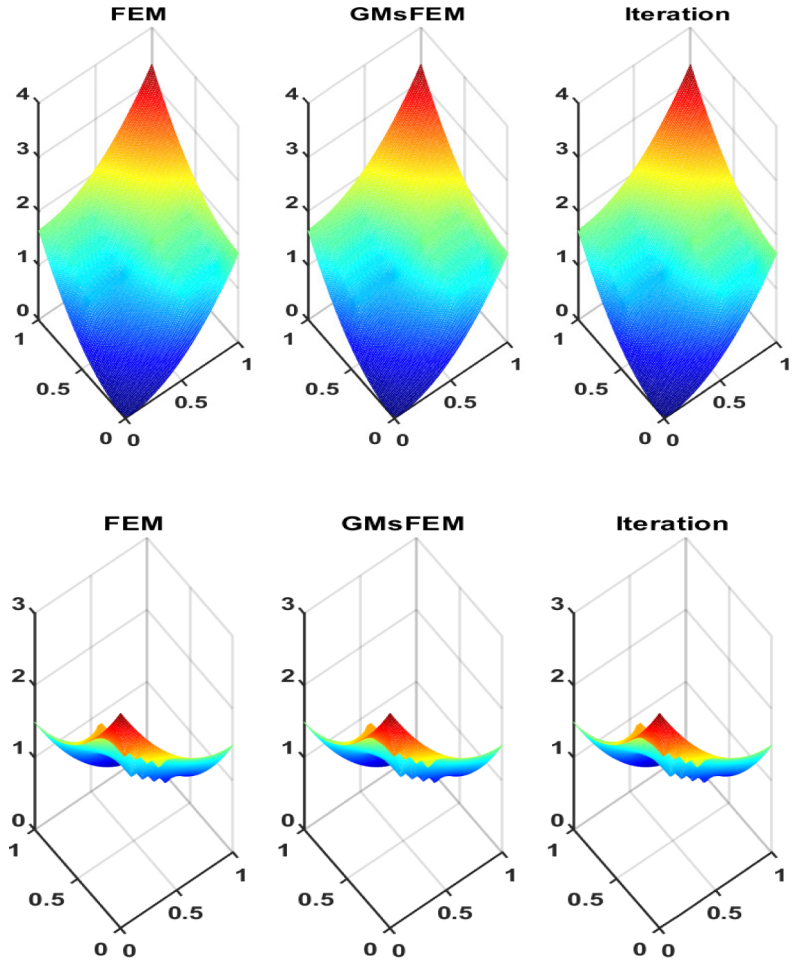

FIG. 3. *Figures of* $p_1(x,\boldsymbol{\xi})$ *(1st row) and* $p_2(x,\boldsymbol{\xi})$ *(2nd row) by different methods.*

where $i = 1, 2$, and the relative errors in the sense of a_Q-norm as

$$\begin{cases} a_q^{\text{gms}} = \dfrac{1}{N}\displaystyle\sum_{j=1}^{N} \dfrac{\|\boldsymbol{p}^{\text{ref}}(x,\boldsymbol{\xi}_j) - \boldsymbol{p}^{\text{gms}}(x,\boldsymbol{\xi}_j)\|_{a_Q}}{\|\boldsymbol{p}^{\text{ref}}(x,\boldsymbol{\xi}_j)\|_{a_Q}}, \\ a_q^{\text{Iter-GMs}} = \dfrac{1}{N}\displaystyle\sum_{j=1}^{N} \dfrac{\|\boldsymbol{p}^{\text{ref}}(x,\boldsymbol{\xi}_j) - \boldsymbol{p}^{\text{Iter-GMs}}(x,\boldsymbol{\xi}_j)\|_{a_Q}}{\|\boldsymbol{p}^{\text{ref}}(x,\boldsymbol{\xi}_j)\|_{a_Q}}, \end{cases} \tag{5.3}$$

where N is the number of parameter samples.

To evaluate the approximation for the proposed iterative method, we randomly choose 500 parameter samples and compute the average L^2 errors. For fixed tolerance $\epsilon = 10^{-8}$, the maximum of iteration number $N_{\text{iter}} = 30$ and the number of local basis functions $L = 5$, the profiles of variables $p_1(x, \boldsymbol{\xi})$ and $p_2(x, \boldsymbol{\xi})$ are all shown in Figure 3. By different methods, the mean for solutions of $p_1(x, \boldsymbol{\xi})$ are plotted in the first row and $p_2(x, \boldsymbol{\xi})$ are plotted in the second row, respectively. From the figure, the moments of variables $p_1(x, \boldsymbol{\xi})$ and $p_2(x, \boldsymbol{\xi})$ using GMsFEM and the proposed iterative method have a good agreement with the reference results.

To discuss the effect of the coarse mesh size, we consider some different coarse mesh sizes in the example, $H = \{1/3, 1/6, 1/8, 1/10, 1/12, 1/24\}$. The relative errors in the sense of L^2 norm and a_Q norm are recorded separately in Tables 1 and 2. In the tables, we can see that the approximation for the state variables $p_1(x, \boldsymbol{\xi})$ and $p_2(x, \boldsymbol{\xi})$ are improved as the coarse mesh become finer.

For different number of local basis functions at each coarse block, Figure 4 depicts the plots of L^2 error and a_Q error against number of local basis functions. With the larger number of local basis functions, it can be seen that both the L^2 error and a_Q error decrease.

To verify the convergence condition of the proposed iterative method, we will change the infimum values of $\kappa_1^0(x)$ and $\kappa_2^0(x)$, that is the conductivity values in the background of Figure 2. In this experiment, we take the supremum of $\kappa_1^1(x, \boldsymbol{\xi})$ and $\kappa_2^1(x, \boldsymbol{\xi})$ as $\overline{\kappa_1^1}(x, \boldsymbol{\xi}) = 7.9402$ and $\overline{\kappa_2^1}(x, \boldsymbol{\xi}) = 7.9269$, respectively. Both the infimum values of $\kappa_1^0(x)$ and $\kappa_2^0(x)$ are set as $\{1, 1.5, 2.5, 3, 6, 8, 20\}$, respectively. In Table 3, we list the relative errors in the sense of L^2 norm and a_Q norm versus different ratios of $\overline{\kappa^1}/\underline{\kappa^0}$. From the table, we can see that when the convergence condition $\underline{\kappa^0} - 2\overline{\sigma}C_p^2 \geq \overline{\kappa^1}$ is once satisfied, the proposed iterative method is converged.

TABLE 1
The relative L^2 errors with different coarse mesh size H for $\boldsymbol{p}(x, \boldsymbol{\xi})$.

Coarse mesh size	$H = 1/3$	$H = 1/6$	$H = 1/8$	$H = 1/10$	$H = 1/12$	$H = 1/24$
$e_p^{1,\text{gms}}$	2.3545E-01	1.2777E-01	1.2234E-01	3.2728E-03	3.3909E-03	8.6720E-04
$e_p^{1,\text{Iter-GMs}}$	1.3163E-01	1.0171E-01	5.0570E-02	2.9348E-03	1.7041E-03	6.9226E-04
$e_p^{2,\text{gms}}$	2.3725E-01	1.2803E-01	1.2281E-01	3.7408E-03	3.8105E-03	1.8348E-03
$e_p^{2,\text{Iter-GMs}}$	1.3149E-01	1.0196E-01	5.1679E-02	3.6918E-03	2.6849E-03	1.9509E-03

TABLE 2
The relative a_q-norm errors with different coarse mesh size H for $\boldsymbol{p}(x, \boldsymbol{\xi})$.

Coarse mesh size	$H = 1/3$	$H = 1/6$	$H = 1/8$	$H = 1/10$	$H = 1/12$	$H = 1/24$
a_q^{gms}	2.4223E+00	9.9258E-01	7.0460E-01	1.1033E-01	9.3013E-02	6.0044E-02
$a_q^{\text{Iter-GMs}}$	2.4150E+00	9.9098E-01	7.0321E-01	1.1048E-01	9.3194E-02	6.0340E-02

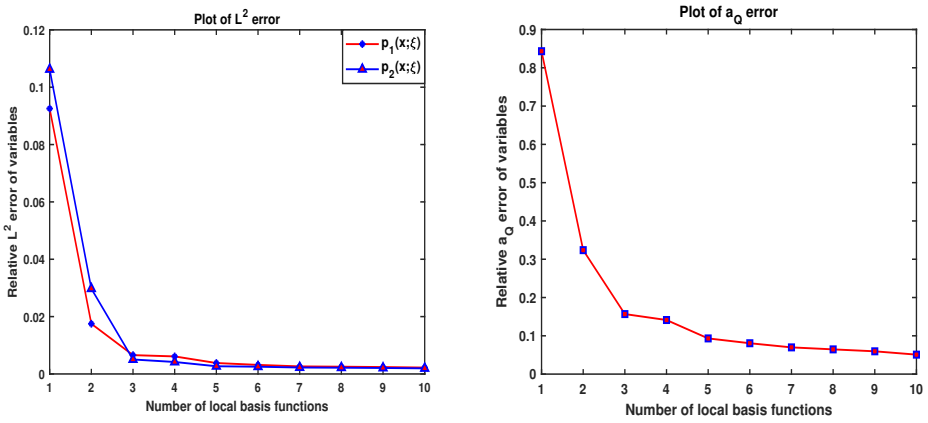

FIG. 4. *Plot for errors in Experiment* 1. *Left:* L^2 *error; Right:* a_Q *error.*

TABLE 3
History of convergence with 5 *basis functions.*

$\overline{\kappa^1}/\underline{\kappa^0}$	$e_p^{1,\mathrm{Iter-GMs}}$	$e_p^{2,\mathrm{Iter-GMs}}$	$a_Q^{\mathrm{Iter-GMs}}$
7.9402	4.3143E + 25	9.7825E + 24	4.0640E + 26
5.2935	3.6451E + 16	2.9900E + 16	5.7810E + 17
3.1761	5.3708E + 04	3.8313E + 05	5.7826E + 06
2.6467	7.9935E + 00	4.7545E + 01	7.1734E + 02
1.3234	5.1564E-03	1.1884E-02	1.0160E-01
0.9925	3.4592E-03	7.7112E-03	9.9733E-02
0.3970	3.8105E-03	2.6849E-03	9.3194E-02

5.2. Experiment 2. In this example, we consider the following dual-continuum model, which is also defined in the unit square $\Omega = [0,1]^2$.

$$
\begin{cases}
-\operatorname{div}(\kappa_1(x,\boldsymbol{\xi})\nabla p_1(x,\boldsymbol{\xi})) + \sigma(x)(p_1(x,\boldsymbol{\xi}) - p_2(x,\boldsymbol{\xi})) = f_1(x,\boldsymbol{\xi}), \ x \in \Omega, \\
\qquad\qquad p_1(x,\boldsymbol{\xi})|_{\partial\Omega} = (1 + 2\boldsymbol{\xi}_1\boldsymbol{\xi}_3)(x_1^2 + x_2^2), \\
-\operatorname{div}(\kappa_2(x,\boldsymbol{\xi})\nabla p_2(x,\boldsymbol{\xi})) - \sigma(x)(p_1(x,\boldsymbol{\xi}) - p_2(x,\boldsymbol{\xi})) = f_2(x,\boldsymbol{\xi}), \ x \in \Omega, \\
\qquad\qquad p_2(x,\boldsymbol{\xi})|_{\partial\Omega} = (1 + \boldsymbol{\xi}_3^3)((x_1 - 1)^2 + (x_2 - 1)^2).
\end{cases} \tag{5.4}
$$

Similar to the first example, the diffusion coefficients $\kappa_i(x,\boldsymbol{\xi})$ $(i = 1,2)$, transfer parameter $\sigma(x)$ and source terms are defined by

$$
\begin{cases}
\kappa_1(x,\boldsymbol{\xi}) = \kappa_1^0(x) + (1 + \xi_1^2\xi_2^2)(1 + x_1^2)x_2, \\
\kappa_2(x,\boldsymbol{\xi}) = \kappa_2^0(x) + (1 + \xi_2^2 + \xi_3^2)(1 + 2x_1 - 2x_1x_2^2)), \\
\sigma(x) = x_1^2x_2^2/2, \\
f_1(x,\xi) = (2\xi_1 + \xi_5^2)(x_1 - x_1^2)(x_2 - x_2^2) + (\xi_1\xi_2\xi_3 + \xi_3\xi_4/5)(x_1 - x_1^2 + x_2 - x_2^2), \\
f_2(x,\boldsymbol{\xi}) = (3 + \xi_2\xi_5)x_2(x_1 - x_2^2) + (1 + 2\xi_3\xi_4))(1 - x_1^2)(1 - 2x_2).
\end{cases}
$$

Here $x = (x_1, x_2) \in \Omega$ and the random vector $\boldsymbol{\xi} := (\xi_1, \xi_2, \cdots, \xi_5)$. Each ξ_i $(i = 1,2,\cdots,5)$ obeys the uniform distribution in $U(0,1)$. The deterministic part in diffusion coefficients $\kappa_1^0(x)$ and $\kappa_2^0(x)$ are both high-contrast functions independent of $\boldsymbol{\xi}$, whose maps are depicted in Figure 5. The conductivity values in the background both are fixed to be 1, while the conductivity values in the channels are 10000 and 10020, respectively. In this experiment, we randomly take 5000 random samples to test the proposed iterative method.

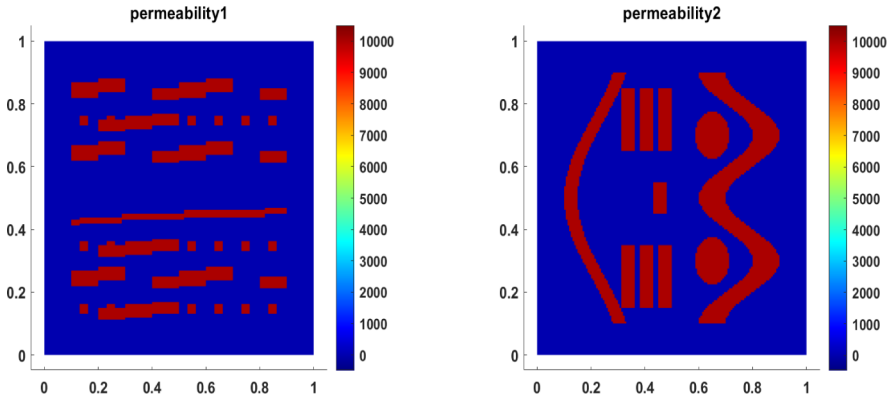

FIG. 5. *High-contrast functions* $\kappa_1^0(x)$ *(left) and* $\kappa_2^0(x)$ *(right).*

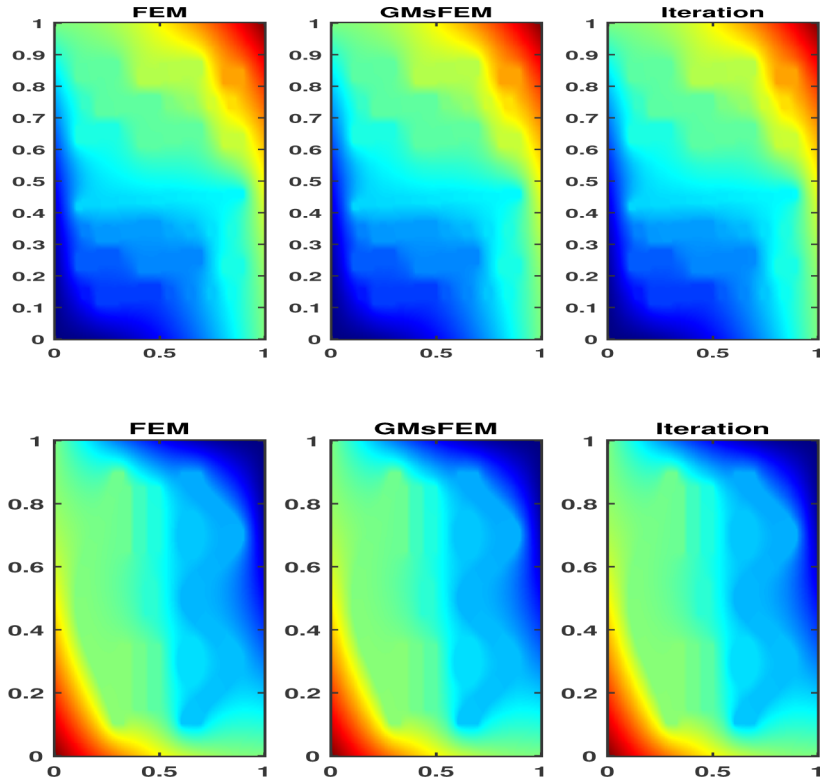

FIG. 6. *Plots of reference solutions and numerical solutions:* $p_1(x,\boldsymbol{\xi})$ *(1st row) and* $p_2(x,\boldsymbol{\xi})$ *(2nd row).*

Figure 6 shows the solutions of the multicontinuum model for the three methods: FEM on 256×256 fine grid (reference solutions), GMsFEM on 16×16 coarse mesh size, and the proposed iterative method. The figure shows that the solutions have very good agreement with the reference solutions for the variables $p_1(x,\boldsymbol{\xi})$ and $p_2(x,\boldsymbol{\xi})$.

To demonstrate the effectiveness of the proposed iterative method, we next define the absolute error in the sense of infinite norm as $\|p_1^{k+1}(x,\boldsymbol{\xi}) - p_1^k(x,\boldsymbol{\xi})\|_\infty + \|p_2^{k+1}(x,\boldsymbol{\xi}) - p_2^k(x,\boldsymbol{\xi})\|_\infty$. In Figure 7, we depict the absolute error for $\boldsymbol{p}(x,\boldsymbol{\xi})$ versus

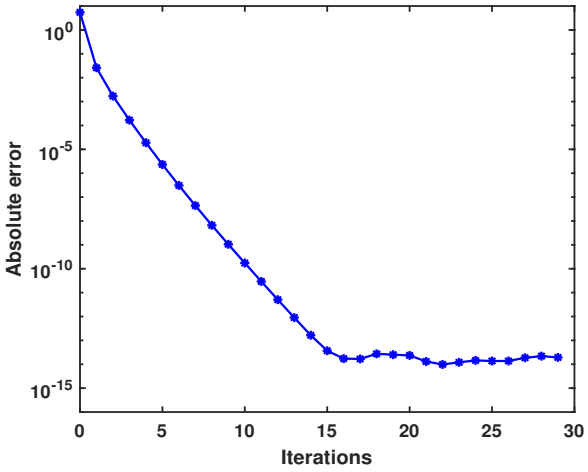

FIG. 7. *Absolute error of the iterations.*

TABLE 4
The relative L^2 errors with different coarse mesh size H for $\boldsymbol{p}(x,\boldsymbol{\xi})$.

Coarse mesh size	$H=1/4$	$H=1/8$	$H=1/16$	$H=1/32$	$H=1/64$
$e_p^{1,\mathrm{Iter-GMs}}$	1.4976E-01	1.2108E-01	2.5186E-03	1.9031E-03	1.6322E-03
$e_p^{2,\mathrm{Iter-GMs}}$	1.2951E-01	1.3118E-01	1.8416E-03	1.2229E-03	6.7742E-04

TABLE 5
History of convergence with $L=5$ local basis functions.

H	a_Q^{gms}	order	$a_Q^{\mathrm{Iter-GMs}}$	order
1/4	2.1541E+00	-	2.1540E+00	–
1/8	9.9206E-01	1.119	9.9205E-01	1.119
1/16	9.1778E-02	4.553	9.1883E-02	4.551
1/32	7.8812E-02	1.591	7.8934E-02	1.590
1/64	4.9649E-02	1.360	4.9840E-02	1.358

the different iteration number. The figure shows the absolute error decreases steadily as the number of iteration increase.

Next we fix the number of local basis functions $L=5$ for each coarse element, the stop criterion $\epsilon = 5\times 10^{-8}$ and the maximum iteration number $N_{\mathrm{iter}}=30$. Table 4 and 5 record the error in L^2 norm and a_Q norm with different coarse mesh sizes.

Both the results in Table 4 and Table 5 show that the numerical approximation are very accurate, and the errors converge with refinement of the coarse mesh size. Moreover, Table 5 verifies convergence rate of the proposed iterative method and GMsFEM with various settings. From the table, we can find the approximation of the iterative method is consistent with GMsFEM. This shows that the proposed iterative method is credible.

As the same way, we will take different sets of the infimum values of $\kappa_1^0(x)$ and $\kappa_2^0(x)$ to verify the convergence condition. In this experiment, we fix the supremum of $\kappa_1^1(x,\boldsymbol{\xi})$ and $\kappa_2^1(x,\boldsymbol{\xi})$ as $\overline{\kappa_1^1}(x,\boldsymbol{\xi})=3.5704$ and $\overline{\kappa_2^1}(x,\boldsymbol{\xi})=7.6735$, respectively. In Table 6, we list the relative errors in L^2 norm and a_Q norm versus different ratios of $\overline{\kappa_1^1}(x,\boldsymbol{\xi})/\underline{\kappa_1^0}(x)$ and $\overline{\kappa_2^1}(x,\boldsymbol{\xi})/\underline{\kappa_2^0}(x)$. Similar to the results in experiment 1, the proposed iterative method will converge as the condition $\underline{\kappa^0}-2\overline{\sigma}C_p^2\geq\overline{\kappa^1}$ is satisfied.

TABLE 6
History of convergence with 6 basis functions.

$\overline{\kappa_1}/\underline{\kappa^0}$	$e_p^{1,\mathrm{Iter-GMs}}$	$e_p^{2,\mathrm{Iter-GMs}}$	$a_Q^{\mathrm{Iter-GMs}}$
7.6735	4.0718E + 08	1.0153E + 12	8.6020E + 12
6.3946	1.7551E + 02	5.9535E + 03	3.5075E + 04
5.1157	2.5502E-01	1.0094E + 01	6.0340E + 01
3.0694	1.1774E-02	2.2079E-03	1.0211E-01
2.5578	1.0245E-02	2.0821E-03	9.9420E-02
1.0962	5.1142E-03	1.8716E-03	9.2698E-02
0.3837	2.5186E-03	1.8416E-03	9.1883E-02

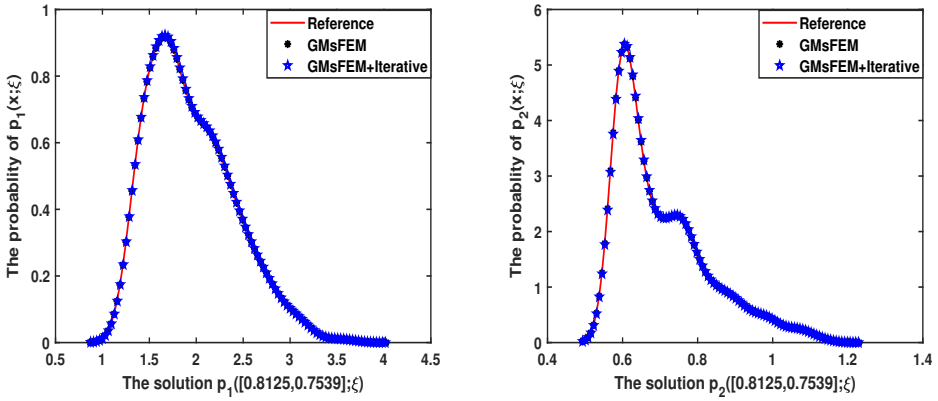

FIG. 8. *Probability density of $p_1(x,\xi)$ and $p_2(x,\xi)$ at one random location for reference, GMsFEM and the iterative method with fixed coarse mesh size and number of local basis functions.*

Based on the reference, GMsFEM and the iterative method, Figure 8 depicts the probability density estimates of $p_1(x,\xi)$ and $p_2(x,\xi)$ at one random location. The figures show that the iterative method renders the same probability density as the references solution and GMsFEM solution.

5.3. Experiment 3. In this subsection, we will present the numerical experiments to show the presented iterative method in the fracture modeling.

$$
\begin{cases}
-\operatorname{div}\left(\kappa_1(x,\boldsymbol{\xi})\nabla p_1(x,\boldsymbol{\xi})\right)+\sigma(x)\left(p_1(x,\boldsymbol{\xi})-p_2(x,\boldsymbol{\xi})\right)=f_1(x,\boldsymbol{\xi}),\ x\in\Omega,\\
\qquad\qquad p_1(x,\boldsymbol{\xi})|_{\partial\Omega}=0,\\
-\operatorname{div}\left(\kappa_2(x,\boldsymbol{\xi})\nabla p_2(x,\boldsymbol{\xi})\right)-\sigma(x)\left(p_1(x,\boldsymbol{\xi})-p_2(x,\boldsymbol{\xi})\right)=f_2(x,\boldsymbol{\xi}),\ x\in\Omega,\\
\qquad\qquad p_2(x,\boldsymbol{\xi})|_{\partial\Omega}=0.
\end{cases}
\tag{5.5}
$$

Here $\kappa_i(x,\xi)$ has fractures with high values and low values in the matrix (see Figure 9 for illustration). In the figure, we depict three fracture fields used in the simulations below. We take the domain Ω to be the unit square, set the forcing terms as

$$
\begin{cases}
\kappa_1^m=10+\cos(\pi x_2)+(2+x_1^2+x_2)(1+2\boldsymbol{\xi}^3+\boldsymbol{\xi}^5),\\
\kappa_2^m=30+\sin(\pi x_1)+(1+x_1+x_2^2+x_1x_2^2)(1+\boldsymbol{\xi}^2+5\boldsymbol{\xi}^4),\\
f_1(x,\xi)=-\pi^2x_2\sin(\pi x_1+\pi x_2)\sin(\pi x_2)(\sin\boldsymbol{\xi}+2\boldsymbol{\xi}^2),\\
f_2(x,\boldsymbol{\xi})=\pi^2(x_1x_2+1)\sin(\pi x_1)\cos(\pi x_2)(2+\boldsymbol{\xi}^2).
\end{cases}
$$

and the transfer term is defined as

$$\sigma(x)=1+\exp(x_1)\sin(x_2^3).$$

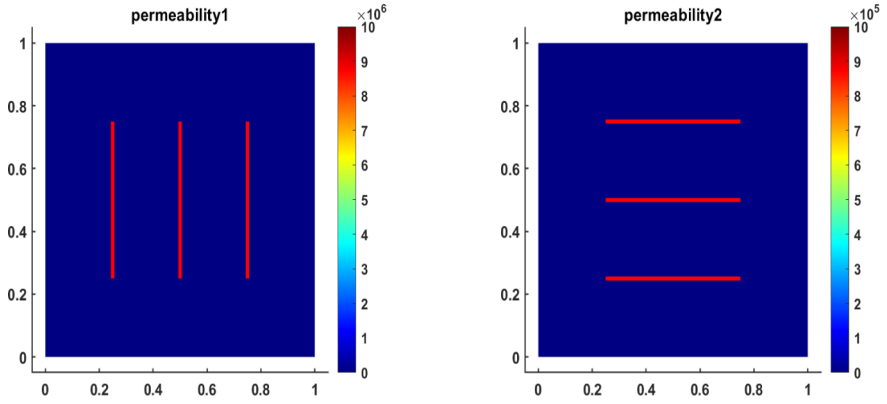

FIG. 9. *Fracture fields* $\kappa_1^f(x)$ *(left) and* $\kappa_2^f(x)$ *(right).*

TABLE 7
The relative L^2 *errors with different coarse mesh size* H *for* $\boldsymbol{p}(x,\boldsymbol{\xi})$.

Coarse mesh size	$H=1/3$	$H=1/6$	$H=1/12$	$H=1/24$
$e_p^{1,\mathrm{Iter-GMs}}$	5.9561E-01	2.5933E-01	5.5257E-02	5.0335E-02
$e_p^{2,\mathrm{Iter-GMs}}$	6.0265E-01	2.1346E-01	1.8119E-02	1.1054E-02

Furthermore, we impose the homogeneous Dirichlet boundary conditions for the dual continuum problem. In our numerical simulations, we use a 12×12 coarse grid, and each coarse grid block is further divided into 10 fine grid blocks. Thus, the whole computational domain is partitioned into a 120×120 fine grid. 1000 random samples are taken to test the proposed iterative method.

Figure 10 shows the solutions of the multicontinuum model for the three methods: FEM on 120×120 fine grid (reference solutions), GMsFEM on 12×12 coarse mesh size and the proposed iterative method. We observe that the iterative solutions are good approximations of the fine-scale solution for the variables $p_1(x,\boldsymbol{\xi})$ and $p_2(x,\boldsymbol{\xi})$. Next we fix the number of local basis functions $L=5$ for each coarse block, the stop criterion $\epsilon = 10^{-8}$, and the maximum iteration number $N_{\mathrm{iter}} = 50$. Table 7 records the error in L^2 norm with different coarse mesh sizes $H = \{1/3, 1/6, 1/12, \frac{1}{2}4\}$. From this table, we see clearly that our method gives a better approximation of the reference solutions as the coarse mesh sizes decreases.

To illustrate the impact of iteration numbers on the algorithm's performance, we present the relative L^2-error convergence in Figure 11 across varying iteration counts. As illustrated in the graph, the relative L^2 errors of the variables show a consistent decreasing trend with increasing the number of iteration, eventually converging to a stable value.

6. Conclusions. In our paper, we have presented an Iter-GMsFEM for solving a parameter-dependent dual continuum model. Our approach leverages the benefits of iterative methods combined with GMsFEM, offering an effective solution strategy for this complex model. Firstly, we reformulated the original problem as another problem with the parameter-independent multiscale coefficient and exchange term and a parameter-dependent right-hand side, a fixed-point iteration is then used to simulate the flow. Due to its highly heterogeneous and high contrast regions, the iterative method to solve the full model would lead much computation burden and

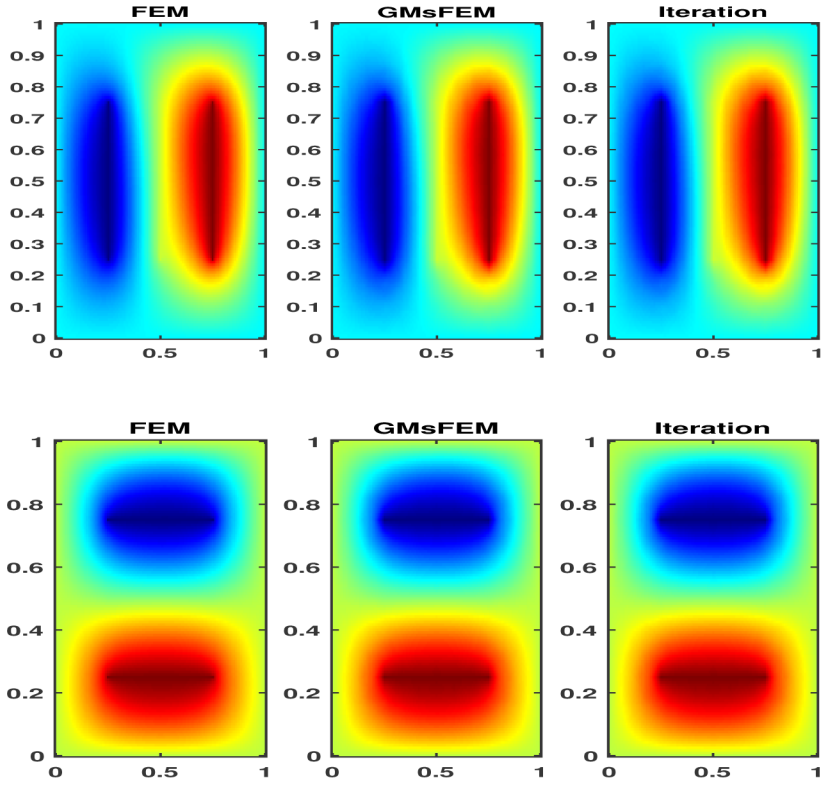

FIG. 10. *Plots of reference solutions and numerical solutions:* $p_1(x,\boldsymbol{\xi})$ *(1st row) and* $p_2(x,\boldsymbol{\xi})$ *(2nd row).*

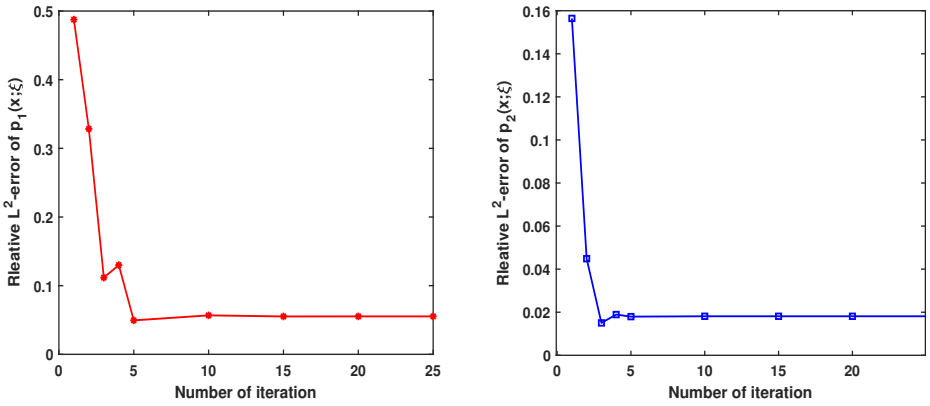

FIG. 11. *Relative* L^2*-error of numerical solutions:* $p_1(x,\boldsymbol{\xi})$ *(left) and* $p_2(x,\boldsymbol{\xi})$ *(right) with different number of iteration.*

huge memory. To this end, we constructed the lower dimensional space by GMsFEM to accelerate the iterative process. The entire computation involves two stage: offline phase and online phase. Based on the reformulation, we just need to calculate the multiscale basis functions for one time in the offline phase. The computation process is divided into two stages: the offline phase and the online phase. During the offline phase, we only need to compute the multiscale basis functions once. In contrast,

the online phase is highly efficient because it leverages the reuse of matrix inverses and model reduction techniques. We have thoroughly derived the optimal error order and validated the efficiency and accuracy of our method through various numerical examples, which confirm the consistency with the theoretical results.

Appendix A. Proof of Lemma 4.5.

Proof. By the Poincaré inequality, there exists a positive constant C_p such that

$$\|v_i\|_{L^2(\Omega)} \leq C_p \|\nabla v_i\|_{L^2(\Omega)},$$

for all $v_i \in H_0^1(\Omega), i = 1, 2$. Thus we obtain

$$\begin{aligned} \|\boldsymbol{v}\|_{a_Q}^2 &\geq \underline{\kappa^0} \|\nabla \boldsymbol{v}\|_{\boldsymbol{L}^2(\Omega)}^2 - 2\overline{\sigma} \|\boldsymbol{v}\|_{\boldsymbol{L}^2(\Omega)}^2 \\ &\geq \underline{\kappa^0} \|\nabla \boldsymbol{v}\|_{\boldsymbol{L}^2(\Omega)}^2 - 2\overline{\sigma} C_p^2 \|\nabla \boldsymbol{v}\|_{\boldsymbol{L}^2(\Omega)}^2 \end{aligned}$$

and

$$\begin{aligned} \|\boldsymbol{v}\|_{a_Q}^2 &\leq \overline{\kappa^0} \|\nabla \boldsymbol{v}\|_{\boldsymbol{L}^2(\Omega)}^2 + 2\overline{\sigma} \|\boldsymbol{v}\|_{\boldsymbol{L}^2(\Omega)}^2 \\ &\leq \overline{\kappa^0} \|\nabla \boldsymbol{v}\|_{\boldsymbol{L}^2(\Omega)}^2 + 2\overline{\sigma} C_p^2 \|\nabla \boldsymbol{v}\|_{\boldsymbol{L}^2(\Omega)}^2. \end{aligned}$$

We deduce that

$$\alpha_0 \|\nabla \boldsymbol{v}\|_{\boldsymbol{L}^2(\Omega)} \leq \|\boldsymbol{v}\|_{a_Q} \leq \beta_0 \|\nabla \boldsymbol{v}\|_{\boldsymbol{L}^2(\Omega)},$$

where $\alpha_0 = (\underline{\kappa^0} - 2\overline{\sigma} C_p^2)^{\frac{1}{2}}$ and $\beta_0 = (\overline{\kappa^0} + 2\overline{\sigma} C_p^2)^{\frac{1}{2}}$ by assumption conditions of section 2. This completes the proof. ∎

Acknowledgments. The authors would like to thank the anonymous referees for their insightful comments on how to improve the quality of this paper. This work was supported by National Key R & D Program of China (2021YFA1001300), National Natural Science Foundation of China (12271150, 12171406, 12101217, 12331011), China Postdoctoral Science Foundation (2022M713875) and Natural Science Foundation of Hunan Province (2022JJ40113).

REFERENCES

[1] I. Y. Akkutlu, Y. Efendiev, M. Vasilyeva, and Y. Wang, *Multiscale model reduction for shale gas transport in a coupled discrete fracture and dual-continuum porous media*, J. Nat. Gas Sci. Eng., 48 (2017), pp. 65–76, https://doi.org/10.1016/j.jngse.2017.02.040.

[2] R. G. Baca, R. C. Arnett, and D. W. Langford, *Modelling fluid flow in fractured-porous rock masses by finite-element techniques*, Internat. J. Numer. Methods Fluids, 4 (1984), pp. 337–348, https://doi.org/10.1002/fld.1650040404.

[3] G. I. Barenblatt, Iu.P. Zheltov, and I. N. Kochina, *Basic concepts in the theory of seepage of homogeneous liquids in fissured rocks [strata]*, J. Appl. Math. Mech., 24 (1960), pp. 1286–1303, https://doi.org/10.1016/0021-8928(60)90107-6.

[4] M. B. G. M. Biermans, K. M. Dijkema, and D. A. De Vries, *Water movement in porous media towards an ice front*, J. Hydrol., 37 (1978), pp. 137–148, https://doi.org/10.1016/0022-1694(78)90102-6.

[5] I. I. Bogdanov, V. V. Mourzenko, J. F. Thovert, and P. M. Adler, *Two-phase flow through fractured porous media*, Phys. Rev. E, 68 (2003), 026703, https://doi.org/10.1103/PhysRevE.68.026703.

[6] S. L. Brunton and J. N. Kutz, *Data-driven Science and Engineering: Machine Learning, Dynamical Systems, and Control*, 2nd ed., Cambridge University Press, Cambridge, 2022.

[7] Z. Chen, G. Huan, and Y. Ma, *Computational Methods for Multiphase Flows in Porous Media*, SIAM, 2006.

[8] S. W. Cheung, E. T. Chung, Y. Efendiev, W. T. Leung, and M. Vasilyeva, *Constraint energy minimizing generalized multiscale finite element method for dual continuum model*, Commun. Math. Sci., 18 (2020), pp. 663–685, https://doi.org/10.4310/CMS.2020.v18.n3.a4.

[9] E. T. Chung, Y. Efendiev, and T. Y. Hou, *Adaptive multiscale model reduction with generalized multiscale finite element methods*, J. Comput. Phys., 320 (2016), pp. 69–95, https://doi.org/10.1016/j.jcp.2016.04.054.

[10] E. T. Chung, Y. Efendiev, and W. T. Leung, *Constraint energy minimizing generalized multiscale finite element method in the mixed formulation*, Comput. Geosci., 22 (2018), pp. 677–693, https://doi.org/10.1007/s10596-018-9719-7.

[11] E. T. Chung, Y. Efendiev, W. T. Leung, and M. Vasilyeva, *Coupling of multiscale and multi-continuum approaches*, GEM Int. J. Geomath., 8 (2017), pp. 9–41, https://doi.org/10.1007/s13137-017-0093-8.

[12] E. T. Chung, Y. Efendiev, W. T. Leung, M. Vasilyeva, and Y. Wang, *Non-local multi-continua upscaling for flows in heterogeneous fractured media*, J. Comput. Phys., 372 (2018), pp. 22–34, https://doi.org/10.1016/j.jcp.2018.05.038.

[13] Y. Efendiev, J. Galvis, and T. Y. Hou, *Generalized multiscale finite element methods (GMsFEM)*, J. Comput. Phys., 251 (2013), pp. 116–135, https://doi.org/10.1016/j.jcp.2013.04.045.

[14] B. Eikemo, K. A. Lie, G. T. Eigestad, and H. K. Dahle, *Discontinuous Galerkin methods for advective transport in single-continuum models of fractured media*, Adv. Water Res., 32 (2009), pp. 493–506, https://doi.org/10.1016/j.advwatres.2008.12.010.

[15] J. Erhel, J. R. de Dreuzy, and B. Poirriez, *Flow simulation in three-dimensional discrete fracture networks*, SIAM J. Sci. Comput., 31 (2009), pp. 2688–2705, https://doi.org/10.1137/080729244.

[16] X. Feng, J. Lin, and C. Lorton, *An efficient numerical method for acoustic wave scattering in random media*, SIAM/ASA J. Uncertain. Quantif., 3 (2015), pp. 790–822, https://doi.org/10.1137/140958232.

[17] X. Feng, J. Lin, and C. Lorton, *A multimodes Monte Carlo finite element method for elliptic partial differential equations with random coefficients*, Int. J. Uncertain. Quantif., 6 (2016), pp. 429–443, https://doi.org/10.1615/Int.J.UncertaintyQuantification.2016016805.

[18] X. Feng and C. Lorton, *An efficient Monte Carlo interior penalty discontinuous Galerkin method for elastic wave scattering in random media*, Comput. Methods Appl. Mech. Engrg., 315 (2017), pp. 141–168, https://doi.org/10.1016/j.cma.2016.10.036.

[19] X. Feng, Y. Luo, L. Vo, and Z. Wang, *An efficient iterative method for solving parameter-dependent and random convection-diffusion problems*, J. Sci. Comput., 90 (2022), pp. 1–26, https://doi.org/10.1007/s10915-021-01737-z.

[20] J. Galvis and Y. Efendiev, *Domain decomposition preconditioners for multiscale flows in high-contrast media*, Multiscale Model. Simul., 8 (2010), pp. 1461–1483, https://doi.org/10.1137/090751190.

[21] S. Geiger, S. Matthäi, J. Niessner, and R. Helmig, *Black-Oil simulations for three-component, three-phase flow in fractured porous media*, SPE J., 14 (2009), pp. 338–354, https://doi.org/10.2118/107485-PA.

[22] S. Granet, P. Fabrie, P. Lemonnier, and M. Quintard, *A two-phase flow simulation of a fractured reservoir using a new fissure element method*, J. Pet. Sci. Eng., 32 (2001), pp. 35–52, https://doi.org/10.1016/S0920-4105(01)00146-2.

[23] M. Gunzburger, N. Jiang, and M. Schneier, *An ensemble-proper orthogonal decomposition method for the nonstationary Navier–Stokes equations*, SIAM J. Numer. Anal., 55 (2017), pp. 286–304, https://doi.org/10.1137/16M1056444.

[24] M. Gunzburger, N. Jiang, and Z. Wang, *An efficient algorithm for simulating ensembles of parameterized flow problems*, IMA J. Numer. Anal., 39 (2019), pp. 1180–1205, https://doi.org/10.1093/imanum/dry029.

[25] J. H. Han, M. Wang, P. Bai, F. R. Brushett, and M. Z. Bazant, *Dendrite suppression by shock electrodeposition in charged porous media*, Sci Rep., 6 (2016), 28054, https://doi.org/10.1038/srep28054.

[26] C. C. Harris, *Sedimentation rates, fluidization and flow through porous media*, Nature, 184 (1959), pp. 716–716, https://doi.org/10.1038/184716a0.

[27] T. Hayat, Z. Hussain, A. Alsaedi, and B. Ahmad, *Numerical study for slip flow of carbon-water nanofluids*, Comput. Methods Appl. Mech. Engrg., 319 (2017), pp. 366–378, https://doi.org/10.1016/j.cma.2017.02.021.

[28] J. S. Hesthaven, G. Rozza, and B. Stamm, *Certified Reduced Basis Methods for Parametrized Partial Differential Equations*, Springer, 2016.

[29] L. Howle, R. P. Behringer, and J. Georgiadis, *Visualization of convective fluid flow in a porous medium*, Nature, 362 (1993), pp. 230–232, https://doi.org/10.1038/362230a0.
[30] N. Jiang and W. Layton, *An algorithm for fast calculation of flow ensembles*, Int. J. Uncertain. Quantif., 4 (2014), pp. 273–301, https://doi.org/10.1615/Int.J.UncertaintyQuantification.2014007691.
[31] H. H. Kim, E. Chung, and J. Wang, *BDDC and FETI-DP preconditioners with adaptive coarse spaces for three-dimensional elliptic problems with oscillatory and high contrast coefficients*, J. Comput. Phys. J., 349 (2017), pp. 191–214, https://doi.org/10.1016/j.jcp.2017.08.003.
[32] G. Li, *On the convergence rates of GMsFEMs for heterogeneous elliptic problems without oversampling techniques*, Multiscale Model. Simul., 17 (2019), pp. 593–619, https://doi.org/10.1137/18M1172715.
[33] Q. Li, Y. Wang, and M. Vasilyeva, *Multiscale model reduction for fluid infiltration simulation through dual-continuum porous media with localized uncertainties*, J. Comput. Appl. Math., 336 (2018), pp. 127–146, https://doi.org/10.1016/j.cam.2017.12.040.
[34] Y. Luo and Z. Wang, *A multilevel Monte Carlo ensemble scheme for random parabolic PDEs*, SIAM J. Sci. Comput., 41 (2019), pp. A622–A642, https://doi.org/10.1137/18M1174635.
[35] S. K. Matthäi, A. Mezentsev, and M. Belayneh, *Finite element-node-centered finite-volume two-phase-flow experiments with fractured rock represented by unstructured hybrid-element meshes*, SPE Reserv. Eval. Eng., 10 (2007), pp. 740–756, https://doi.org/10.2118/93341-PA.
[36] J. S. R. Park, S. W. Cheung, T. Mai, and V. H. Hoang, *Multiscale simulations for upscaled multi-continuum flows*, Int. J. Comput. Appl. Math., 374 (2020), 112782, https://doi.org/10.1016/j.cam.2020.112782.
[37] D. M. Pedroso, *A solution to transient seepage in unsaturated porous media*, Comput. Methods Appl. Mech. Engrg., 285 (2015), pp. 791–816, https://doi.org/10.1016/j.cma.2014.12.009.
[38] A. Quarteroni, A. Manzoni, and F. Negri, *Reduced Basis Methods for Partial Differential Equations: An Introduction*, Springer, 2015.
[39] A. E. Scheidegger, *The Physics of Flow Through Porous Media*, University of Toronto Press, 1957.
[40] B. R. Scanlon, R. E. Mace, M. E. Barrett, and B. Smith, *Can we simulate regional groundwater flow in a karst system using equivalent porous media models? Case study, Barton Springs Edwards aquifer, USA*, J. Hydrol., 276 (2003), pp. 137–158, https://doi.org/10.1016/S0022-1694(03)00064-7.
[41] M. Ţene, M. S. Al Kobaisi, and H. Hajibeygi, *Algebraic multiscale method for flow in heterogeneous porous media with embedded discrete fractures (F-AMS)*, J. Comput. Phys., 321 (2016), pp. 819–845, https://doi.org/10.1016/j.jcp.2016.06.012.
[42] Y. S. Wu and K. Pruess, *A multiple-porosity method for simulation of naturally fractured petroleum reservoirs*, Spe Reservoir Eng., 3 (1988), pp. 327–336, https://doi.org/10.2118/15129-PA.
[43] D. Xiao, F. Fang, C. C. Pain, and I. M. Navon, *A parameterized non-intrusive reduced order model and error analysis for general time-dependent nonlinear partial differential equations and its applications*, Comput. Methods Appl. Mech. Engrg., 317 (2017), pp. 868–889, https://doi.org/10.1016/j.cma.2016.12.033.
[44] B. Yan, M. Alfi, A. Cheng, Y. Cao, Y. Wang, and J. E. Killough, *General multi-porosity simulation for fractured reservoir modeling*, J. Nat. Gas Sci. Eng., 33 (2016), pp. 777–791, https://doi.org/10.1016/j.jngse.2016.06.016.
[45] S. Zhang, Z. Yang, and X. Guan, *Multi-modes multiscale approach of heat transfer problems in heterogeneous solids with uncertain thermal conductivity*, Adv. Appl. Math. Mech., 15 (2023), pp. 69–93, https://doi.org/10.4208/aamm.OA-2022-0048.